# Tunable Dual-Band THz Metamaterial Absorber with Regression-Learning-Enabled Numerical Redesign

Sumaia Jahan Mishu[1,2], Yaser Mike Banad[1], Sarah Sharif[1,2,*]
[1]*Department of Electrical and Computer Engineering, The University of Oklahoma*
Norman, Oklahoma, USA
[2]*Centre for Quantum Research and Technology, The University of Oklahoma*
Norman, Oklahoma, USA
*Corresponding Author Email: s.sh@ou.edu

***Abstract*—Terahertz (THz) metamaterial absorbers have garnered considerable interest for applications in sensing, detection, and stealth technologies due to their capacity to achieve engineered absorption at subwavelength scales. This study introduces a high-performance THz metamaterial absorber featuring integrated circular split-ring resonators patterned in copper over a lead glass substrate. The design achieves dual strong absorption peaks at approximately 1.44 THz and 4.24 THz, each with absorption amplitudes nearing 90%. To explore the influence of geometric parameters on absorption characteristics and facilitate predictive modeling, full-wave electromagnetic simulations were performed by systematically varying key design variables. The resulting dataset comprises geometric parameters as input features and corresponding resonant frequencies and absorption amplitudes as target outputs. Two machine learning strategies were employed: forward design, predicting spectral response from geometry, and inverse design, estimating geometry from desired frequency peaks. Multiple linear and tree based regression models, including linear, lasso, random forest, decision trees, gradient boosting models were trained and evaluated using standard error metrics such as RMSE, MAE, and $R^2$ etc. A physics-informed confirmation step was carried out by re-simulating specific regression-predicted designs in a full-wave solver and comparing the resulting resonance frequencies and absorption levels with the intended targets, producing low percentage errors. Because the inverse design approach allows for the immediate retrieval of geometry corresponding to user-specified resonance frequencies and absorption amplitudes, facilitating quick spectrum-to-structure design, this validation further illustrates the tunability of the suggested absorber. All things considered, the suggested data-driven methodology reduces dependency on computationally costly repetitive simulations by facilitating effective optimization and quick prototyping of THz absorbers.**

***Index Terms*—Metamaterial, absorber, random forest, gradient boost, decision trees, regression**

## I. Introduction

Metamaterials are artificially engineered structures designed to exhibit electromagnetic properties not typically found in natural materials. These properties arise from their subwavelength periodic architecture rather than the intrinsic characteristics of their constituent materials [1]–[4]. By tailoring unit cell geometries and arrangements, metamaterials can achieve exotic phenomena such as negative permittivity, negative permeability, and negative refractive index. These capabilities have led to a wide range of applications, including cloaking, superlensing, perfect absorption, and advanced antenna designs [5]–[9].

The terahertz (THz) frequency range, typically spanning from 0.1 to 10 THz, lies between the microwave and infrared regions of the electromagnetic spectrum. This region has attracted significant interest due to its unique potential in non-invasive imaging, chemical sensing, high-speed wireless communications, and security screening [10]–[15]. However, the development of efficient devices in this range is challenging due to the lack of naturally occurring materials with strong THz responses. As a result, metamaterial-based solutions offer a compelling approach for designing functional THz components with customizable spectral characteristics [16]–[19]. This controllability can be further enhanced by incorporating phase-change materials into the metamaterial architecture. For instance, phase change materials-based multifunctional reconfigurable terahertz metamaterials have been explored for joint polarization control, demonstrating how these platforms can provide additional flexibility for dynamically tunable THz wave manipulation [20]–[22].

Among the various metamaterial applications, absorbers that exhibit near-unity absorption at target frequencies have shown particular promise in the THz regime [23]–[25]. THz metamaterial absorbers utilize tailored resonant structures, such as split-ring resonators, to confine and dissipate incident THz energy effectively [26]–[28]. These absorbers are especially useful in stealth technology, thermal imaging, biosensing, and spectroscopic applications. Dual-band or multiband absorbers are of special interest due to their ability to target multiple spectral features within a compact footprint. Recent studies have continued to expand the capabilities of terahertz metamaterials toward both reconfigurable and sensing-oriented applications. In parallel, polarization-insensitive terahertz metamaterial absorbers have also been developed for sensing applications, where the absorber performance is optimized through full-wave electromagnetic simulation and geometric parameter analysis [29], [30]. These studies reflect the growing interest in THz metamaterials for multifunctional control, robust absorption, and sensing performance.

Recent advancements in machine learning (ML) have further accelerated the design and optimization of metamaterials and metasurfaces [31]–[35]. ML techniques are increasingly being integrated with simulation workflows to predict electromagnetic responses [36]–[39], reverse-engineer geometric parameters, and explore high-dimensional design spaces efficiently [40]–[43]. By training regression models on simulation datasets, researchers can significantly reduce computational costs and enable real-time design iterations for functional electromagnetic devices [44]–[46]. Advances in intelligent electromagnetic design have significantly expanded the scope of terahertz metasurface research beyond conventional trial-and-error optimization. In particular, recent reviews have highlighted the rapid growth of machine-learning-assisted metasurface design strategies for complex electromagnetic structures [47]. At the terahertz scale, recent studies have demonstrated inverse-design and deep-learning-based frame- works for multifunctional THz metasurfaces, efficient on-demand THz metasurface synthesis, and high-Q THz metamaterial design with both forward and inverse neural modeling [48]–[50]. These developments indicate a clear shift in the field toward data-driven and intelligent design methodologies for THz devices.

Within this broader landscape, the present study addresses a more focused but practically relevant problem, the forward and inverse design of a passive dual-band THz metamaterial absorber within a bounded geometric parameter space. Unlike generalized inverse-design frameworks aimed at highly multifunctional metasurfaces or large-scale component synthesis, the proposed approach emphasizes a compact regression-based workflow using a small set of physically interpretable geometric inputs, comparative evaluation across multiple regressors, and full-wave re-simulation to verify the inverse-predicted structures.

The broader feasibility of machine-learning-assisted multiband absorber design is demonstrated in [51]. The main focus in [52] was on benchmarking several regression models for forward prediction of absorber performance, and search-based structural optimization through a multi-objective firefly algorithm rather than a trainable inverse-design workflow was developed in [53]. In contrast, this study combines a compact merged circular split-ring resonator geometry with both forward and inverse regression in a single unified pipeline. It is designed around a small set of physically meaningful geometric parameters, multiple train/test split evaluations, and several complementary error metrics, followed by full-wave re-simulation of the inverse-predicted structures for physical verification. Therefore, the key contribution of this work is not simply higher predictive accuracy or faster optimization alone, but the establishment of a low-complexity, computationally efficient, and physically validated spectrum-to-geometry design strategy for passive dual-band THz metamaterial absorbers.

THz metamaterial absorbers have demonstrated a wide range of functionalities, including dual-band response, multiband operation, tunability, and high-sensitivity sensing; however, the literature still shows a persistent tradeoff between spectral performance, structural simplicity, and design efficiency. Passive dual-band absorbers generally rely on carefully engineered metallic resonators and repeated full-wave parametric optimization, which can provide strong absorption performance but are not inherently suitable for rapid inverse redesign from target spectral requirements [54], [55]. By contrast, graphene and other active-material-based absorbers enable tunability and multifunctionality, but often at the cost of additional material, electrical biasing, and fabrication complexity [56], [57]. In parallel, machine-learning-assisted design strategies have shown strong potential for accelerating absorber development through surrogate prediction, inverse mapping, and parameter optimization [51]–[53]. Despite these advances, relatively few studies combine a structurally simple passive dual-band absorber with a closed-loop forward and inverse design framework and full-wave revalidation of inverse-predicted geometries. In this context, the present work addresses that gap by integrating a compact dual-band absorber design with regression-based forward and inverse modeling, followed by electromagnetic re-simulation to confirm the physical reliability of the predicted geometries for practical spectrum-to-structure redesign [51].

The remainder of the paper is organized as follows. Section II describes the metamaterial unit-cell design and full-wave simulation setup. Section III discusses the electromagnetic characterization and material properties at the resonant frequencies. Section IV presents the equivalent circuit interpretation of the two resonance modes, and Section V analyzes the field and current distributions to explain the physical origin of absorption.

Section VI details the parametric study and dataset generation procedure, while Section VII presents the regression-learning framework and model training strategy. Section VIII reports the forward-design performance for predicting $(f_1, f_2, A_1, A_2)$ from geometry, and Section IX presents the inverse-design results for estimating the required geometry from desired spectral targets. Section X then provides a physics-informed confirmation by re-simulating multiple inverse-predicted geometries in the full-wave solver, extracting the achieved resonance peaks and absorption amplitudes, and computing percentage errors with respect to the desired targets. This validation also demonstrates the rendered tunability of the absorber, since the regression-based inverse mapping enables selecting geometries to realize user-specified resonance frequencies and absorption levels without repeated trial-and-error sweeps. Section XI discusses about fabrication and probable experimental process. Finally, Section XII concludes the paper with key findings and future directions.

## II. Design and Simulation of the Metamaterial Unit Cell

The structural design analyzed in this study is illustrated in Fig. 1(a) and Fig. 1(b). Inspired by previous works that employed combinations of multiple split-ring resonator (SRR) elements, this work adopts a fundamental absorber design framework using integrated circular ring resonators to realize a high-performance THz metamaterial absorber [24]. The proposed structure consists of a square-shaped lead glass dielectric substrate with copper layers at the top and bottom, each with a thickness of 0.1 um. The unit cell consists of two concentric circular split-ring resonators which forms a larger split ring resonator together patterned on the top copper layer within a square unit-cell of side length (40 $\mu$m). The geometric parameters defining this structure are: $I$ (15.5 $\mu$m) and $O$(13.6 $\mu$m) (inner and outer radii of the larger ring), $IS$ (4 $\mu$m) and $IO$ (1.8 $\mu$m) (inner and outer radii of the smaller ring), and $S$ (1.2 $\mu$m) (split-gap length). These parameters fully specify the resonator geometry used throughout the parametric and regression analyses. The resonators feature circular gaps with a split separation. The copper layer possesses an electrical conductivity of $5.96 \times 10^7$ S/m, while the dielectric permittivity of the lead glass is taken as 6. The simulation setup, shown in Fig. 1(b), involves 3D frequency-domain analysis using FEM-based electromagnetic software. The unit cell is illuminated by a TE-polarized THz plane wave with the electric field aligned along the z-axis. Floquet-port boundary conditions are applied along x and y directions to model periodicity, and open boundaries are defined along the z-axis to simulate free-space propagation. The principal simulation parameters and

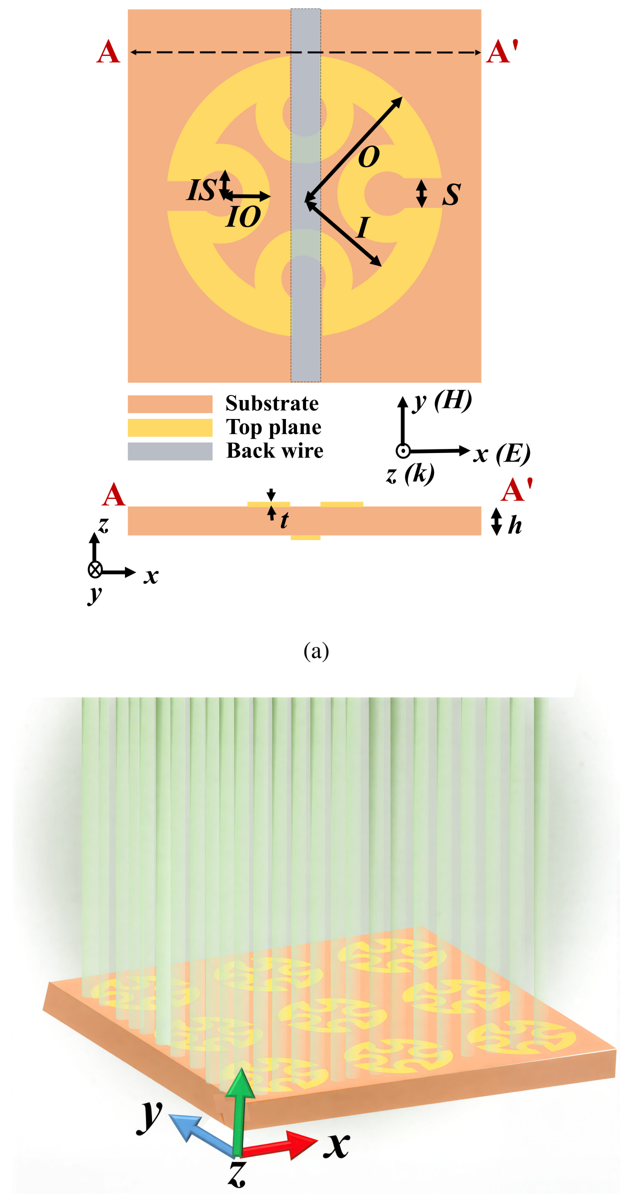


Fig. 1: (a) Geometry of the proposed dual-band THz metamaterial absorber, consisting of merged circular split-ring resonators patterned on a copper–lead-glass unit cell. (b) Simulation setup used for full-wave electromagnetic analysis, showing TE-polarized plane-wave incidence, applied Floquet boundary conditions, and open boundaries along the propagation axis

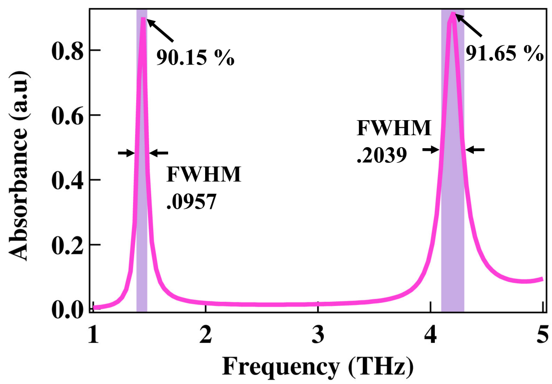


Fig. 2: Simulated absorption spectrum of the proposed metamaterial absorber across the THz frequency range, showing two strong absorption peaks near 1.45 THz and 4.24 THz with absorption exceeding 90%.

numerical conditions adopted for the electromagnetic analysis of the proposed THz metamaterial absorber are summarized in TABLE II. The simulation results demonstrate more than 90% absorption at two THz frequencies as shown in Fig. 2 which are attributed to resonant behaviour characteristics characterized by effective material properties.

The absorption of the proposed metamaterial absorber can be calculated directly from the simulated scattering parameters. Under plane-wave excitation, the reflected and transmitted power ratios are given by $R(\omega) = |S_{11}(\omega)|^2$ and $T(\omega) = |S_{21}(\omega)|^2$, respectively. Hence, the absorptance is obtained from energy conservation as,

$$A(\omega) = 1 - R(\omega) - T(\omega) = 1 - |S_{11}(\omega)|^2 - |S_{21}(\omega)|^2 . \tag{1}$$

To quantify the spectral selectivity of the proposed dual-band THz metamaterial absorber, the full width at half maximum (FWHM) of each absorption resonance was extracted from the simulated absorption spectrum (Fig. 2). A narrower FWHM indicates stronger frequency selectivity, which is beneficial for multi-band filtering and sensing applications.

For the first absorption band centered at $f_1 \approx 1.45$ THz, the measured linewidth is $\mathrm{FWHM}_1 \approx 0.0957$ THz. For the second band centered at $f_2 \approx 4.24$ THz, the linewidth is $\mathrm{FWHM}_2 \approx 0.2039$ THz. Using the standard definition of the loaded quality factor,

$$Q = \frac{f_0}{\mathrm{FWHM}}, \tag{2}$$

the corresponding quality factors are calculated as,

$$Q_1 = \frac{f_1}{\mathrm{FWHM}_1} = \frac{1.45}{0.0957} \approx 15.15,$$

$$Q_2 = \frac{f_2}{\mathrm{FWHM}_2} = \frac{4.24}{0.2039} \approx 20.79.$$

TABLE I: Summary of simulation parameters and numerical conditions used in this study.

| Parameter | Characterization |
|---|---|
| Operating range | THz regime |
| Solver type | Frequency-domain electromagnetic solver |
| Frequency sweep range | 0.5- 5 THz |
| Unit-cell configuration | Periodic metamaterial absorber unit cell |
| Boundary conditions | periodic boundary conditions in the $x$- and $y$-directions |
| Propagation direction | Incident wave along the $z$-direction |
| Excitation type | Normally incident plane wave |
| Polarization condition | Linearly polarized wave |
| Fixed geometrical parameters | Outer radius of big CSRR, structural dimension of the unit cell square |
| Geometrical input variables | Inner and outer radii of small CSRR, split gap length, inner radii of big CSRR |
| Absorber configuration | Metal–dielectric–metal structure |
| Geometrical input variables | Inner and outer redius of the resonators, split gap etc. |
| Output responses | Resonance frequencies and absorption amplitudes |
| Ambient condition | Air |
| Temperature | 300 K |

These results indicate that the higher-frequency resonance exhibits a larger $Q$ factor (narrower normalized linewidth), implying stronger frequency selectivity at $\sim$ 4.24 THz, while both resonances maintain high absorptance ($> 90\%$) with well-defined, sharp spectral features.

While the retrieved effective parameters in Fig. 3 clearly show that both $\epsilon_r$ and $\mu_r$ attain negative values near the two resonant frequencies, it is important to emphasize that perfect absorption does not fundamentally require simultaneous negativity of permittivity and permeability. High absorption in metamaterial absorbers is achieved when the structure satisfies the impedance-matching condition, ensuring suppressed reflection, together with sufficient intrinsic loss to dissipate the transmitted energy. Many high-performance THz absorbers therefore operate without exhibiting double-negative (DNG) behavior. In the present design, however, the coexistence of strong electric and magnetic resonances naturally leads to overlapping regions where both $\epsilon_r$ and $\mu_r$ become negative. Rather than being a strict requirement, this DNG-like response facilitates impedance matching across both bands and strengthens field confinement within the merged circular split-ring

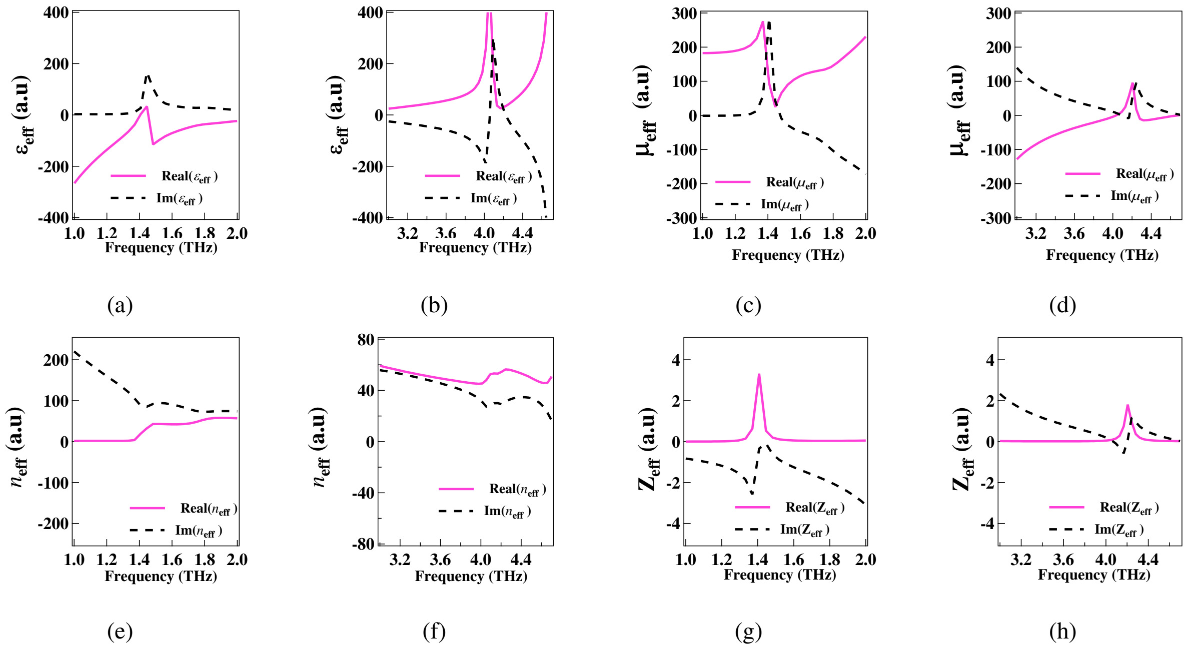


Fig. 3: Retrieved effective electromagnetic parameters of the absorber at 1.44 and 4.24 THz, respectively, (a), (b) effective permittivity $\epsilon(\omega)$, (c), (d) effective permeability $\mu(\omega)$, (e),(f) refractive index n($\omega$), and (g), (h) normalized impedance Z($\omega$). Negative values of $\epsilon$ and $\mu$ and impedance matching at the resonant frequencies confirm dual-band metamaterial absorption behavior.

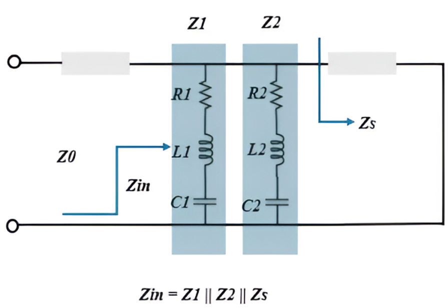


Fig. 4: Equivalent LC circuit model representing the two resonant modes of the metamaterial unit cell. The extracted inductance and capacitance values accurately reproduce the simulated resonant frequencies.

resonators, thereby enabling the dual-band ¿90% absorption demonstrated in this work.

## III. Electromagnetic Characterization and Material Properties of the Absorber

The retrieved effective permittivity ($\varepsilon$) plots reveal that the metamaterial exhibits strong electric resonance behavior at two distinct frequency bands. In both the 1.2–2.0 THz and 3.0–4.8 THz ranges, the real part of permittivity ($\varepsilon_r$) becomes highly negative around 1.45 THz and 4.25 THz, respectively. These sharp dips are accompanied by corresponding peaks in the imaginary part ($\varepsilon_{im}$), indicating strong dielectric losses near resonance. The negative permittivity confirms that the structure supports plasmonic-like electric resonance, an essential feature for artificial materials engineered to exhibit unusual electromagnetic responses.

The effective permeability ($\mu$) plots further highlight the magnetic response of the unit cell. Around the same resonant frequencies (approximately 1.45 THz and 4.25 THz), the real part of permeability ($\mu_r$) also becomes negative, and the imaginary part ($\mu_{im}$) shows significant peaks. This indicates that the unit cell not only supports electric resonance but also exhibits magnetic resonance, likely due to the inclusion of split-ring or other magnetically responsive elements in the structure. The coexistence of negative $\varepsilon_r$ and $\mu_r$ at these frequencies suggests that the material behaves as a double-negative (DNG) metamaterial, which is key to achieving perfect absorption or negative-index behavior.

The effective refractive index ($n$) further supports this observation. In both frequency bands, the real part of the refractive index ($n_r$) becomes negative near the resonant peaks, confirming negative-index metamaterial behavior. The imaginary part of the index ($n_{im}$) is elevated at resonance, indicating increased loss and absorption. These features are consistent with strong

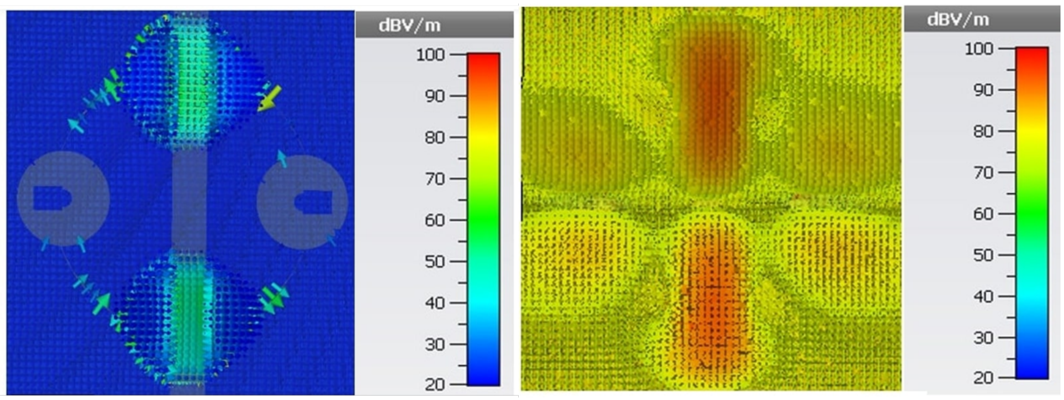


(a)

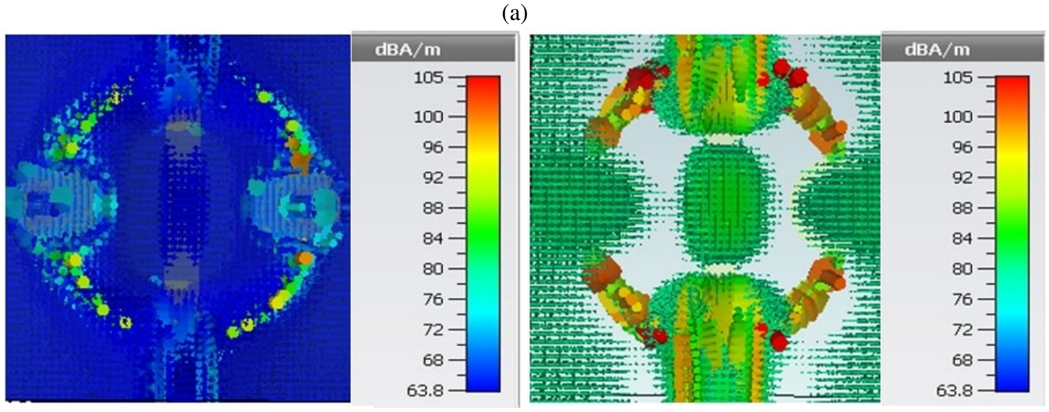


(b)

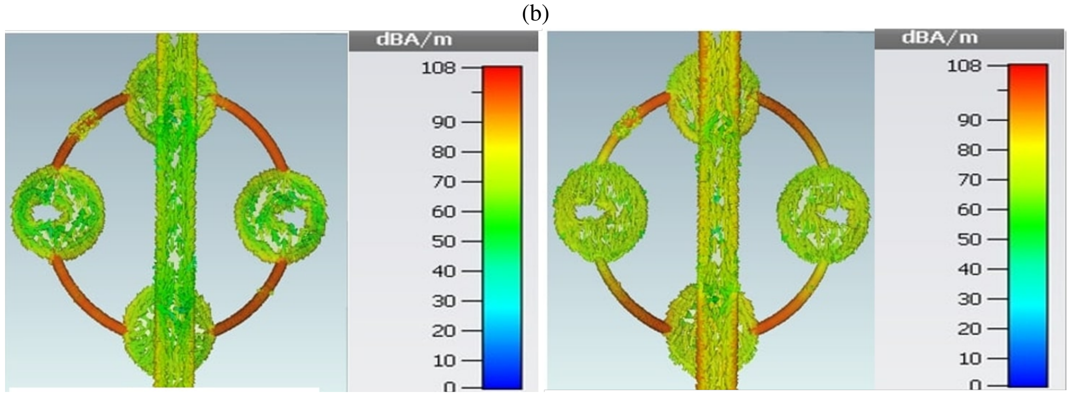


(c)

Fig. 5: Field and current distributions at the two resonant frequencies 1.24 and 4.24 THz respectively, (a) electric field magnitude, (b) magnetic field intensity, and (c) surface current density. The distributions illustrate fundamental and higher-order resonance modes responsible for dual-band absorption.

TABLE II: Comparison of the proposed dual-band THz metamaterial absorber with representative designs from the literature, summarizing material composition, geometry, unit-cell size, resonance frequencies, and application domains.

| **Attribute** | **[58]** | **[59]** | **[60]** | **[61]** | **[62]** | **Proposed work** |
|---|---|---|---|---|---|---|
| **Metamaterial structure** | Orthogonal coupled split-ring metal resonator | Cross-shaped metamaterial layer | Anisotropic graphene strips | Hybrid bi-element resonator | Nested split-ring + wire resonators | Merged circular ring resonators |
| **Conductive layer** | Al, $VO_2$ | $VO_2$, Au, Graphene | Graphene | Graphene, STO | Au | Cu |
| **Number of peaks** | 2 | 2 | Multi-band | 1 | 2 | 2 |
| **Unit cell size ($\mu$m)** | 100×100 | 130×130 | 50×50 | 60×60 | 33×33 | 40×40 |
| **Peak frequencies (THz)** | 0.67, 0.87 | 0.474, 0.831 | 2.1, 2.74, 5.56 | 0.85 | 0.89, 1.36 | 1.44, 4.24 |
| **Application** | Phase transition | Tunability and switching | Selective absorption | Broadband modulation performance at THz | High-Q sensing | THz sensing |
| **Selectivity** | Yes | No | Yes | Yes | Yes | Yes |
| **Tunability** | Yes | Yes | No | Yes | No | Yes |
| **Physics-informed inverse-design confirmation** | No | No | No | No | No | Yes |

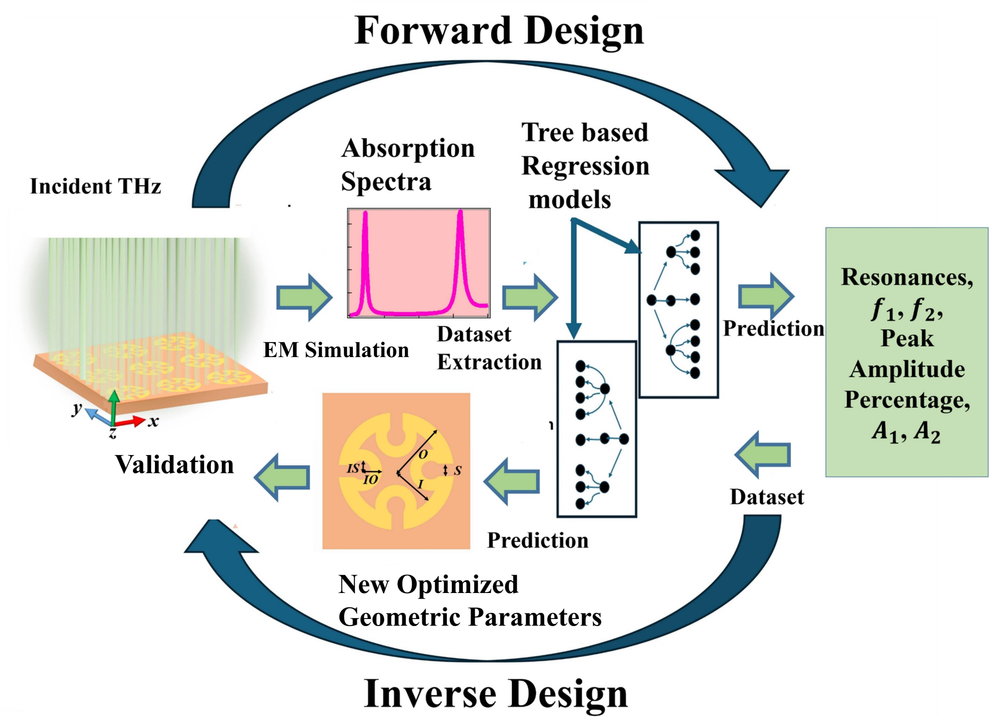


Fig. 6: Design workflow of the proposed regression based predictive modeling of the metamaterial absorber.

dispersion and electromagnetic field confinement near the resonant frequencies, allowing the metamaterial to manipulate wave propagation in unconventional ways.

Lastly, the effective impedance ($Z$) behavior shows that the unit cell is well-matched to free space at the resonant frequencies. At both 1.45 THz and 4.25 THz, the real part of the impedance approaches unity, and the imaginary part nears zero. This condition of impedance matching is crucial for minimizing reflection at the air–metamaterial interface and achieving maximum energy transfer into the absorber. Together, these retrieved parameters confirm that the designed metamaterial unit cell operates as a dual-band perfect absorber with tailored electric and magnetic responses that support resonance, loss, and impedance matching in the THz domain.

## IV. Equivalent circuit Modeling

The two observed resonances at approximately 1.445 THz and 4.244 THz can be interpreted as follows: At 1.445 THz, the equivalent circuit comprises an inductance $L_1 \approx 8.29 \times 10^{-12}$ H in series with a capacitance

$C_1 \approx 1.44 \times 10^{-15}$ F [63]–[65]. Inserting these values into the resonant frequency formula,

$$f_0 = \frac{1}{2\pi\sqrt{LC}} \tag{3}$$

yields $f_0 \approx 1.456$ THz, which closely matches the observed resonance. This confirms that the first resonance corresponds to the fundamental LC mode determined by the physical layout of the metamaterial unit cell [66]–[68].

The higher-order resonance at 4.244 THz is attributed to a distinct LC mode, likely arising from sub-structures or parasitic elements within the unit cell. Using $L_2 = 5.488 \times 10^{-12}$ H and $C_2 = 2.646 \times 10^{-16}$ F, the calculated resonance frequency is approximately $4.176$ THz, which is again in strong agreement with the observed value. This behavior mirrors dual-resonance phenomena found in SRR- or wire-based absorbers [65].

In both cases, the LC equivalent circuit model shown in Fig. 4 predicts the resonant frequencies with less than 2% error and provides an effective means for tuning these responses through geometric or material modifications.

## V. Field Distribution Analysis

At the resonant frequency of 1.44 THz, the electric field distribution is strongly concentrated at the ends of the vertical arms of the resonator, with pronounced intensity near the capacitive gaps as shown in Fig. 5(a). The field pattern is symmetric and indicates a fundamental dipolar resonance mode, where charges oscillate vertically along the resonator. This localization suggests dominant capacitive coupling, storing electric energy between adjacent metal edges. The high electric field magnitude (up to 138 dBV/m) confirms strong confinement, and the structure behaves like an LC circuit with a large capacitive component at this frequency. In contrast, at the higher resonance of 4.24 THz, the electric field becomes more complex, with hotspots distributed at the center and along multiple lobes of the resonator. This pattern reflects a higher-order mode, involving more intricate coupling across the resonator arms. The spread and shape of the field indicate multi-arm interactions and a mixture of capacitive and inductive behavior due to the smaller effective wavelength. Though the color scale differs (up to 100 dBV/m), the relative field intensities show that energy is still effectively trapped, enabling strong absorption. Together, these two resonant behaviors confirm that the metamaterial absorber is engineered to interact efficiently at multiple THz frequencies by supporting distinct electric resonance modes.

At the resonant frequency of 1.44 THz, the magnetic field distribution reveals strong confinement around the curved outer edges of the resonator arms as shown in

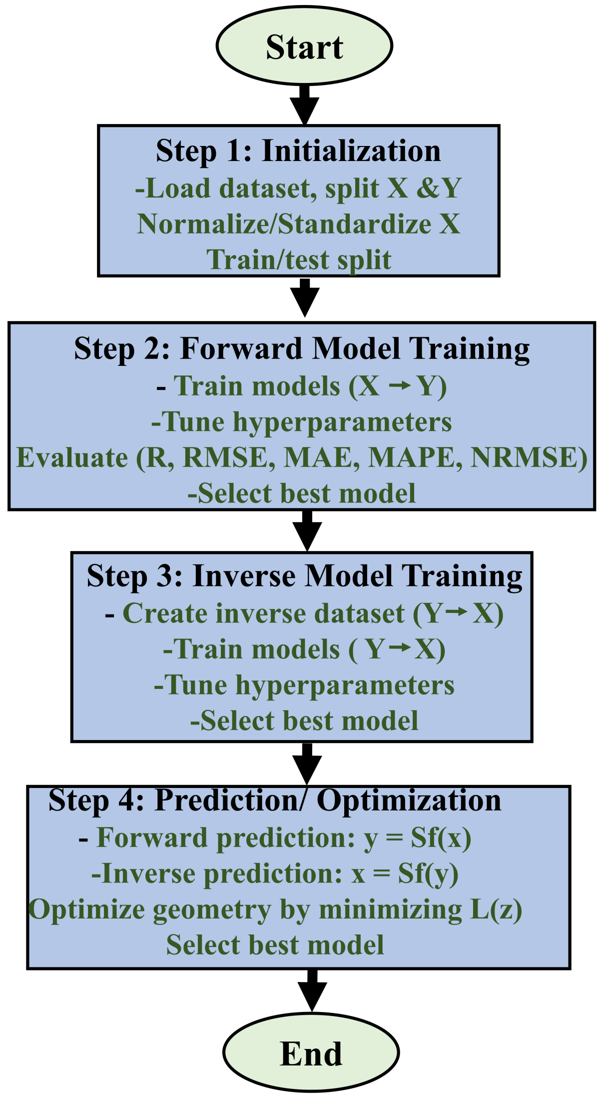


Fig. 7: Regression-based prediction pipeline for forward and inverse design of the metamaterial absorber. The diagram summarizes model training, hyperparameter tuning, feature–target mapping, and prediction stages.

Fig 5(b). The pattern exhibits symmetry and circular concentration on both sides, forming loop-like structures indicative of magnetic dipole resonance. These loops are a result of induced circulating surface currents, which generate magnetic flux and are concentrated primarily in the dielectric spacer between the top resonator and the ground plane. The peak magnetic field intensity reaches around 105 dBA/m, showing that magnetic energy is efficiently stored in these regions, consistent with the inductive behavior of an LC resonator at low frequency. At 4.24 THz, the magnetic field becomes more distributed and intense along the central and diagonal branches of the resonator, with higher-order rotational symmetry

TABLE III: Regression-based forward and inverse design algorithm used for surrogate modeling of the metamaterial absorber. The table summarizes dataset structure, model selection, training steps, evaluation criteria, and optimization workflow

**Regression-Based Forward and Inverse Design Algorithm**

**Input:**

– Dataset $\mathcal{D} = \{(x^{(n)}, y^{(n)})\}_{n=1}^{N}$ where $x^{(n)} = [I, IS, IO, S]$ (geometric parameters) and $y^{(n)} = [f_1, f_2, A_1, A_2]$ (resonant frequencies and amplitudes)
– Train/test split ratio $r$
– Candidate regression models $M = \{\text{Linear}, \text{Lasso}, \text{DT}, \text{RF}, \text{GB}\}$
– Error metrics: $R^2$, RMSE, MAE, MAPE, NRMSE

**Steps:**

**1. Initialization:**
– Load dataset $\mathcal{D}$; split into feature matrix $X$ and target matrix $Y$.
– Normalize or standardize $X$ if needed.
– Split into training and testing sets using ratio $r$.

**2. Forward Model Training:**
For each target $y_k \in Y$:
- Train all models $m \in M$ on $X \to y_k$.
- Tune hyperparameters (e.g., GridSearchCV).
- Evaluate models using $R^2$, RMSE, MAE, MAPE, NRMSE.
- Select best model $m_k^{\star}$.

Store chosen models as forward surrogate $\mathcal{S}_f = \{m_{f_1}^{\star}, m_{f_2}^{\star}, m_{A_1}^{\star}, m_{A_2}^{\star}\}$.

**3. Inverse Model Training:**
– Build inverse dataset $\mathcal{D}_i = \{(y^{(n)}, x_i^{(n)})\}$ where $x_i = [I, IS, IO, S]$.
For each inverse target $x_i$:
- Train models $m \in M$ on $Y \to x_i$.
- Tune hyperparameters and select best model $m_i^{\star}$.

Store chosen models as inverse surrogate $\mathcal{S}_i = \{m_I^{\star}, m_{IS}^{\star}, m_{IO}^{\star}\, m_S^{\star}\}$.

**4. Prediction / Optimization:**
– Forward prediction: For a new geometry $x^*$, compute $\hat{y} = \mathcal{S}_f(x^*)$.
– Inverse prediction: For a target response $y^*$, compute $\hat{x}_i = \mathcal{S}_i(y^*)$.
– (Optional) Optimize geometry by minimizing

$$\mathcal{L}(x) = w_f\left[(\hat{f}_1 - f_1)^2 + (\hat{f}_2 - f_2)^2\right] + w_A\left[(\hat{A}_1 - A_1)^2 + (\hat{A}_2 - A_2)^2\right].$$

using global or Bayesian optimization with $\mathcal{S}_f$ as surrogate.

**5. Repeat or Terminate:**
– If metrics meet tolerance, stop.
– Otherwise, add new samples to $\mathcal{D}$, retrain surrogates, and repeat Steps 2–4.

**Output:**
– Trained forward surrogate $\mathcal{S}_f$ (geometry $\to$ response)
– Trained inverse surrogate $\mathcal{S}_i$ (response $\to$ geometry)
– (Optional) Optimized geometry $x^{\dagger}$ achieving target response

and field flow along multiple curved paths. This more intricate distribution indicates a higher-order magnetic resonance, where multiple inductive loops are activated simultaneously. Although the color scale peaks lower at 90 dBA/m, the relative field enhancement is significant, especially near the junctions of structural arms, highlighting areas of strong magnetic flux density. These patterns confirm that at this frequency, the absorber engages more complex inductive coupling, contributing to strong absorption by capturing energy through multiple resonant pathways.

At the resonant frequency of 1.44 THz, the surface current distribution shows strong and directed current flow along the vertical connector and circular side resonators as illustrated in Fig. 5(c). The current loops around the outer circular arms and flows vertically through the central bar, forming closed-loop patterns. This indicates the formation of a magnetic dipole, where circulating currents induce magnetic flux. The current intensity peaks near the junctions and edges, confirming efficient energy coupling at this fundamental mode. The anti-parallel currents between the top layer and ground plane (not shown) are expected to support strong magnetic resonance, contributing to effective absorption at this frequency. At the higher resonance of 4.24 THz, the surface current becomes more distributed and complex, with visible loops extending along multiple branches of the circular resonators. The current flows both vertically and radially around the arms, indicating a higher-order resonance mode with multi-path current loops. These intricate patterns suggest that multiple resonance pathways are engaged simultaneously, enhancing energy trapping and absorption. The elevated current density along the curved paths and resonator edges reflects strong electromagnetic interaction, enabling efficient suppression of reflection through destructive interference at the surface.

Compared to the earlier designs presented in TABLE II, the proposed merged circular ring resonator demonstrates clear advantages in structural simplicity in using less materials and layers. While the orthogonal coupled split-ring design by [58] achieves dual peaks at frequencies (0.67 and 0.87 THz) for phase-transition applications and the cross-shaped structure by [59] supports tunability with peaks at 0.474 and 0.831 THz, they both rely on more complex conductive materials such as $VO_2$, Au, or graphene. The hybrid bi-element resonator of [61] offers a single broadband peak at 0.85 THz for modulation performance. In contrast, our proposed absorber achieves dual resonances at higher THz frequencies (1.44 THz and 4.24 THz) using a simpler copper-based merged ring design, making it more suitable for compact THz sensing applications. This combination of compact geometry, and simple metal composition underlines the novelty and enhanced practicality of the proposed structure.

## VI. Parametric Study and Dataset Generation

To analyze the influence of geometrical parameters on the absorption characteristics of the metamaterial absorber, a comprehensive parametric sweep was conducted. Four key geometric parameters of the integrated CSRR structure were systematically varied across a defined range to explore their impact on resonance behavior. In this work, the machine-learning dataset was generated from a total of 400 full-wave electromagnetic simulations by systematically varying four key geometric parameters within predefined physically meaningful ranges. This procedure provided representative coverage of the feasible absorber design space while excluding geometrically invalid configurations. Because the input space is limited to four direct geometric variables, the resulting learning problem remains comparatively low-dimensional and physically interpretable.

The inner radius of the small circular resonators (IS) was swept from 0.5 to 3.5 $\mu$m, while the outer radius (IO) was varied from 2.5 to 4.9 $\mu$m. For the larger circular resonator, the inner radius (I) ranged from 12.5 to 17.5 $\mu$m. In addition, the split length (S) of the resonators was varied from 0.2 to 3 $\mu$m. Each of these parameters was sampled linearly, with 100 points in each range, to ensure adequate coverage of the design space. Although changing the inner and outer radii of a ring may appear to represent a similar geometric modification (i.e., adjusting ring thickness), we observed significant spectral and absorption changes when varying the small resonator radii (IS and IO). Therefore, it is important to treat IS and IO as independent parameters for the smaller resonators, since this preserves sensitivity to both the absolute radius and effective ring width, which together strongly influence the resonant response. However, the full factorial combination of these ranges naturally includes some unphysical geometries, for example, cases where the inner radius of the small ring (IS) exceeds the corresponding outer radius (IO). These infeasible configurations were not simulated. Instead, the complete list of parameter combinations was generated first, and only the geometrically valid cases satisfying IO $\geq$ IS were retained for electromagnetic simulation. As a result, the total number of realizable samples reduced to 373, reflecting the elimination of non-physical geometries as well as other numerical-stability exclusions. This approach preserves the independence of the parameter sweeps while ensuring that the dataset used for machine-learning modeling consists solely of physically meaningful resonator structures.

For every unique combination of the five geometric variables, a full-wave electromagnetic simulation was performed using a finite-element solver. A total of 500 unique simulations were executed to generate a comprehensive dataset. From each simulation, the frequency positions of the first and second resonance peaks were extracted along with their corresponding absorption amplitudes. These values serve as the target outputs for forward ML studies, while the geometric parameters constitute the input features.

This dataset serves as the foundation for both forward and inverse design tasks. In the forward approach, the objective is to predict the resonant frequencies and absorption amplitudes from known geometric configurations. Conversely, in the inverse design, desired resonance frequencies are used to infer the appropriate geometric parameters needed to achieve them.

## VII. Machine Learning-Based Modeling

The probabilistic modeling of the metamaterial absorber in this study is based on five geometric parameters as features, with the outputs being the resonance frequencies and absorption amplitudes at two resonances. Five regression models were employed: Linear Regression, Lasso Regression, Decision Tree Regression, Random Forest Regression, and Gradient Boosting Regression.

With the dataset consisting of 400 simulations, the regression task is comparatively well conditioned as only four direct geometric parameters are used as input features. This is fundamentally different from high-dimensional spectrum-based datasets [69], where many sampled frequency points are treated as separate input columns, often increasing feature dimensionality and inter-feature redundancy. In the present case, the target outputs are reduced spectral descriptors, namely the resonance frequencies and corresponding absorption amplitudes, rather than the full absorption spectrum. To assess generalization and reduce the likelihood of overfitting, model performance was evaluated using multiple train–test split ratios of 80:20, 70:30, and 60:40. The consistent performance trends across these different partitions indicate that the stronger-performing models learned stable relationships between geometric inputs and spectral responses rather than memorizing a single subset of the data. Furthermore, the inverse-design predictions were revalidated through full-wave electromagnetic simulation, providing an additional physics-based check on the reliability of the learned mapping.

Linear Regression models the relationship between inputs and outputs by minimizing the residual sum of squares between observed and predicted values. The prediction function is:

$$\hat{y} = \mathbf{w}^\top \mathbf{x} + b \tag{4}$$

where $y$ and $x$ terms are targets and features with $w$ referring to weights with $b$ bias.

In expanded scalar form, the linear regression model becomes:

$$\hat{y} = b + w_1 I + w_3 IS + w_4 IO + w_5 S, \tag{5}$$

where $b$ is the intercept term, $I$ and $O$ denote the inner and outer radii of the larger circular resonator, $IS$ and $IO$ represent the inner and outer radii of the smaller circular resonator, and $S$ is the split length of the resonator.

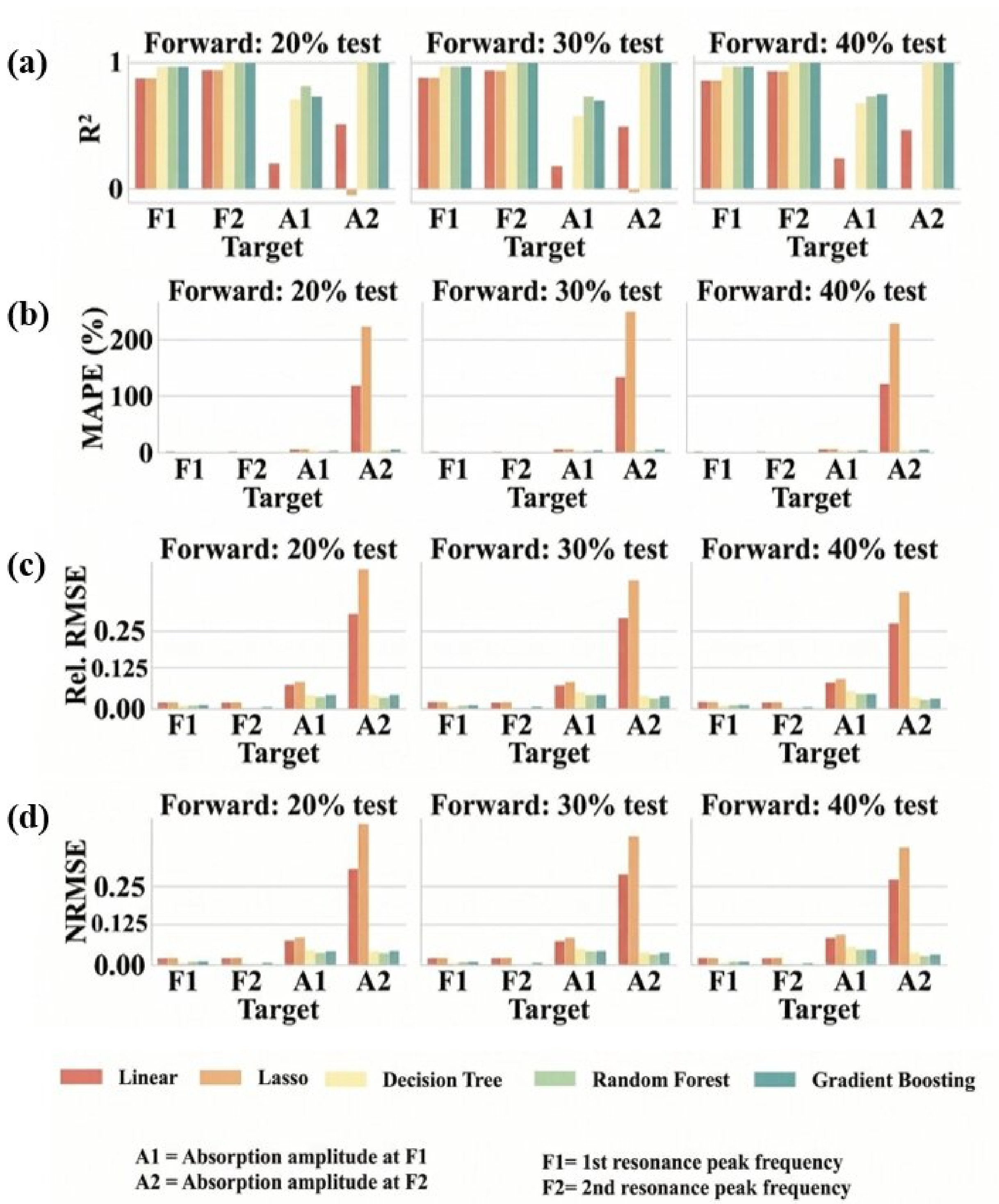


Fig. 8: Forward-design performance metrics across different regression models for multiple train–test splits. The plots compare the accuracy of predicting resonant frequencies and absorption amplitudes from geometric parameters

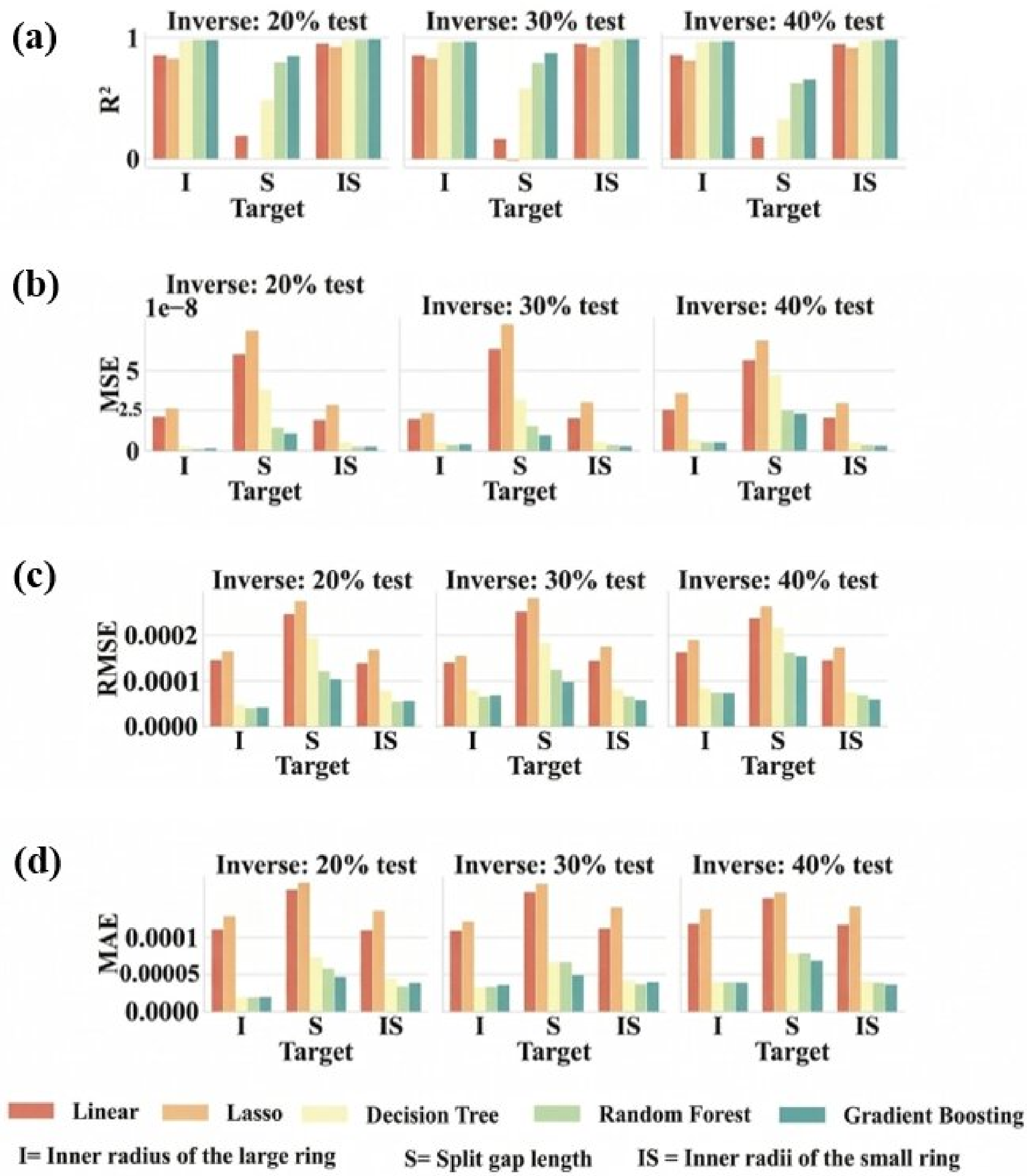


Fig. 9: Inverse-design performance metrics for predicting geometric parameters from target spectral responses using different regression models and test-set ratios. Ensemble models demonstrate the highest accuracy and stability

Lasso Regression extends Linear Regression by adding an regularization term to encourage sparsity in the coefficients and reduce overfitting [70]:

$$\mathcal{L}_{\text{Lasso}} = \sum_{i=1}^{n} \left(y_i - \mathbf{w}^\top \mathbf{x}_i\right)^2 + \lambda\|\mathbf{w}\|_1 \tag{6}$$

Decision Tree Regression partitions the feature space into regions and assigns each region the average of the training outputs that fall within it [71]. Random Forest Regression is an ensemble of $T$ decision treesn [72]:

$$\hat{f}_{\text{RF}}(\mathbf{x}) = \frac{1}{T}\sum_{t=1}^{T} f_t(\mathbf{x}) \tag{7}$$

Gradient Boosting Regression builds an additive model in a forward stage-wise fashion, fitting each new learner to the negative gradient of the loss function [73]:

$$\hat{f}(\mathbf{x}) = \sum_{m=1}^{M} \gamma_m h_m(\mathbf{x}) \tag{8}$$

The performance of these models is evaluated using various metrics: coefficient of determination ($R^2$), mean squared error (MSE), root mean squared error (RMSE), mean absolute error (MAE), mean absolute percentage error (MAPE), relative root mean squared error (Rel. RMSE) and normalized root mean squared error (NRMSE) etc.

The coefficient of determination is:

$$R^2 = 1 - \frac{\sum_{k=1}^{n}(y_k - \hat{y}_k)^2}{\sum_{k=1}^{n}(y_k - \overline{y})^2} \tag{9}$$

The mean squared error (MSE) is:

$$\text{MSE} = \frac{\sum_{k=1}^{n}(y_k - \hat{y}_k)^2}{n} \tag{10}$$

The root mean squared error (RMSE) is:

$$\text{RMSE} = \sqrt{\frac{\sum_{k=1}^{n}(y_k - \hat{y}_k)^2}{n}} \tag{11}$$

The mean absolute error (MAE) is:

$$\text{MAE} = \frac{\sum_{k=1}^{n}|y_k - \hat{y}_k|}{n} \tag{12}$$

The mean absolute percentage error (MAPE) is:

$$\text{MAPE} = \frac{100}{n}\sum_{k=1}^{n}\left|\frac{y_k - \hat{y}_k}{y_k}\right| \tag{13}$$

The relative root mean squared error (Rel. RMSE) is:

$$\text{Rel. RMSE} = \frac{\text{RMSE}}{\overline{y}} \tag{14}$$

where $\overline{y}$ is the mean of the observed values.

These metrics were chosen to provide both absolute and relative measures of prediction error. $R^2$ assesses the proportion of variance explained by the model, indicating the overall goodness of fit. MSE, RMSE, and MAE quantify the absolute magnitude of errors, with RMSE penalizing larger deviations more heavily. MAPE expresses errors as percentages, facilitating comparison across targets of different scales. Rel. RMSE normalizes RMSE by the mean of the observed data, making it scale-independent and suitable for comparing predictions across targets with different magnitudes. The flowchart of the study is presented in Fig.6 and Fig. 7.

## VIII. Forward Design Performance

We evaluated five regression models,Linear Regression, Lasso Regression, Decision Tree, Random Forest, and Gradient Boosting, for predicting the two resonance peaks $(f_1, f_2)$ and their absorption amplitudes $(A_1, A_2)$ from the geometric parameters $(I, O, IS, IO, S)$. The performance summary is reported in TABLE IV and visual examples for different percentage of test datasets are shown in Fig 8.

Four complementary metrics are reported; the coefficient of determination ($R^2$), Normalized RMSE (NRMSE), Mean Absolute Percentage Error (MAPE), and Relative RMSE. We include $R^2$ to quantify explained variance (model fit). NRMSE and Relative RMSE normalize errors by the target scale (range or mean), enabling fair comparisons across targets with very different magnitudes. MAPE expresses error in percent, which is directly interpretable for practitioners. This combination is particularly important here because some targets (the frequencies ) are large in absolute value (THz); even when $R^2$ indicates an excellent fit, raw errors like RMSE or MAE can look numerically large simply due to scale. Using normalized/relative metrics removes this artifact and reflects the true predictive quality.

Across targets, tree-based ensembles outperform linear models. Random Forest and Gradient Boosting achieve the highest $R^2$ and the lowest NRMSE/Relative RMSE for $f_1$ and $A_2$; $f_2$ and $A_1$ are more nonlinear and thus relatively harder, but ensembles still lead. Decision Trees are competitive yet less robust than ensembles, while Linear/Lasso models underfit the nonlinear dependencies between geometry and response.

## IX. Inverse Design Performance

For inverse design, we predict geometric parameters from the electromagnetic response. Based on sensitivity analysis and stability, we focus on $I$, $S$, and $IS$ as targets, using $(f_1, f_2, A_1, A_2)$ as inputs as shown in TABLE V and Fig. 9. We deliberately exclude parameters with near-constant values (e.g., $O$, $IO$) to avoid ill-posed learning and degenerate error metrics. Because electromagnetic inverse problems are generally non-unique, the inverse-design task in this work

TABLE IV: Forward design performance of regression models for predicting resonance frequencies and absorption amplitudes from geometric parameters for 20% test set

| **Metric / Model** | **Linear** | **Lasso** | **Decision Tree** | **Random Forest** | **Gradient Boosting** |
|---|---|---|---|---|---|
| *1st resonance frequency prediction (f1, THz)* | | | | | |
| $R^2$ | 0.9067 | 0.8961 | 0.9343 | 0.9747 | 0.9641 |
| NRMSE | 0.0737 | 0.0777 | 0.0618 | 0.0834 | 0.0457 |
| MAPE (%) | 1.35 | 1.27 | 0.87 | 0.49 | 0.59 |
| Rel. RMSE | 0.0176 | 0.0148 | 0.0597 | 0.0553 | 0.0331 |
| *2nd resonance frequency prediction (f2, THz)* | | | | | |
| $R^2$ | 0.2048 | 0.2048 | 0.6400 | 0.8427 | 0.7626 |
| NRMSE | 0.1664 | 0.1664 | 0.1119 | 0.0740 | 0.0976 |
| MAPE (%) | 6.84 | 6.84 | 4.55 | 2.93 | 3.84 |
| Rel. RMSE | 0.0897 | 0.0897 | 0.0593 | 0.0553 | 0.0638 |
| *Absorption amplitude at 1st resonance (A1, %)* | | | | | |
| $R^2$ | 0.2005 | 0.2007 | 0.5998 | 0.8094 | 0.7223 |
| NRMSE | 0.1879 | 0.1879 | 0.1330 | 0.0972 | 0.1108 |
| MAPE (%) | 6.62 | 6.43 | 4.79 | 2.94 | 3.81 |
| Rel. RMSE | 0.0788 | 0.0788 | 0.0526 | 0.0410 | 0.0414 |
| *Absorption amplitude at 2nd resonance (A2, %)* | | | | | |
| $R^2$ | 0.5116 | 0.5115 | 0.9811 | 0.9926 | 0.9884 |
| NRMSE | 0.2279 | 0.2283 | 0.0438 | 0.0274 | 0.0343 |
| MAPE (%) | 11.22 | 11.26 | 6.19 | 3.97 | 6.00 |
| Rel. RMSE | 0.3041 | 0.3041 | 0.0468 | 0.0526 | 0.0468 |

is formulated in a constrained rather than unrestricted manner. Instead of seeking an arbitrary metasurface geometry from a desired response, the inverse mapping is limited to a single absorber topology within a bounded and fabrication-relevant geometric space. The inverse model is constrained using multiple physical response quantities simultaneously, namely the two resonance frequencies $(f_1, f_2)$ and the corresponding absorption amplitudes $(A_1, A_2)$, which reduces ambiguity compared with matching only one spectral feature. Moreover, based on sensitivity and stability considerations, only the most informative geometric parameters are predicted in the inverse stage, while weakly varying parameters are excluded to avoid ill-posed learning and degenerate solutions. During dataset construction, non-physical geometries are removed, and the final inverse-predicted structures are further checked by full-wave electromagnetic re-simulation. The inverse-design framework mitigates non-uniqueness by restricting the problem to a bounded fabrication-feasible absorber topology, using multiple spectral targets $(f_1, f_2, A_1, A_2)$ as simultaneous constraints, screening the inverse outputs to the most sensitive geometric parameters, and verifying predicted solutions through full-wave re-simulation [74]

Here we report $R^2$, RMSE, and MAE (in the original geometric units). Unlike the forward case, target ranges for geometry are modest, so absolute-error metrics are naturally interpretable and stable; normalized errors (e.g., NRMSE, MAPE) can become misleading when target ranges are very small or values approach zero. Ensembles (Random Forest, Gradient Boosting) again yield the best performance, often achieving $R^2 \gtrsim 0.98$ with very small RMSE/MAE for $I$ and $IS$. The parameter $S$ remains more challenging—consistent with its weaker sensitivity to the available response features—yet ensemble models still provide the most reliable predictions. Linear and Lasso regressions trail due to their limited capacity to capture nonlinear inverse mappings.

The forward design experiments, conducted with 20%, 30%, and 40% test splits, reveal consistent trends across evaluation metrics such as $R^2$, MSE, RMSE, MAE, MAPE, and Relative RMSE. For predicting the resonance frequencies and absorption amplitudes from geometric parameters, ensemble-based models such as Random Forest and Gradient Boosting consistently achieved the highest $R^2$ scores (often exceeding 0.95 for certain targets) and the lowest error metrics across all test sizes. In contrast, linear and lasso regression models showed weaker performance, particularly for parameters exhibiting nonlinear relationships with the outputs. Increasing

TABLE V: Inverse design performance of regression models for predicting geometric parameters from frequency and amplitude targets for 20% test set

| Metric / Model | Linear | Lasso | Decision Tree | Random Forest | Gradient Boosting |
|---|---|---|---|---|---|
| *Prediction of large resonator size (l)* | | | | | |
| $R^2$ | 0.8638 | 0.8271 | 0.9386 | 0.9903 | 0.9899 |
| MSE ($\times 10^{-8}$) | 2.117 | 2.688 | 3.193 | 1.506 | 1.709 |
| RMSE ($\times 10^{-4}$) | 1.46 | 1.64 | 1.79 | 1.23 | 1.31 |
| MAE ($\times 10^{-4}$) | 1.11 | 1.29 | 1.10 | 0.99 | 1.02 |
| *Prediction of cut (S)* | | | | | |
| $R^2$ | 0.1911 | -0.9045 | 0.4897 | 0.8064 | 0.8556 |
| MSE ($\times 10^{-8}$) | 6.045 | 7.521 | 3.818 | 1.448 | 1.080 |
| RMSE ($\times 10^{-4}$) | 2.246 | 2.746 | 1.954 | 1.204 | 1.040 |
| MAE ($\times 10^{-4}$) | 1.65 | 1.87 | 0.77 | 0.51 | 0.47 |
| *Prediction of small resonator size (lS)* | | | | | |
| $R^2$ | 0.9564 | 0.9352 | 0.9816 | 0.9934 | 0.9932 |
| MSE ($\times 10^{-8}$) | 1.927 | 2.861 | 1.635 | 0.292 | 0.299 |
| RMSE ($\times 10^{-4}$) | 1.39 | 1.69 | 1.28 | 0.54 | 0.55 |
| MAE ($\times 10^{-4}$) | 1.10 | 1.35 | 0.46 | 0.33 | 0.38 |

the test set size generally led to a slight reduction in model accuracy for all approaches, as reflected by marginal increases in RMSE and MAPE, although the effect was less pronounced for the ensemble models, demonstrating their superior generalization capability.

In the inverse design tasks, where the goal was to predict geometric parameters from the resonance frequencies and absorption amplitudes, a similar performance hierarchy emerged. Random Forest and Gradient Boosting again dominated in $R^2$ scores and maintained low error rates across different test splits, indicating robustness in capturing the complex, often many-to-one mappings from outputs to inputs. Decision Tree regression performed moderately well but exhibited greater variability in performance as the test set size increased. Linear and lasso regressions struggled with the inverse mapping, often producing higher MSE and MAPE values, especially for larger test sets. Notably, the inclusion of Relative RMSE and MAPE provided a more scale-independent view of the errors—important because the target parameters span large numerical ranges, making traditional metrics like MSE or RMSE alone insufficient for fair comparison.

All test sizes show incredibly low errors for Resonant Frequency 1 and 2 and amplitude 2 prediction. A near-perfect fit for all the targets using tree based regression models are shown by an R2 value that is extremely close to 1 for all test sizes. Stable MAE and MAPE: The model appears to have tiny forecast errors from actual values, as indicated by the Mean Absolute Percentage Error (MAPE) staying below 0.004%.

For Resonant Frequency 2, the RMSE is higher (for example, 0.1842, 20% test size). Relatively higher prediction errors are also confirmed by the MSE and MAE figures. As the test size grows, the negative R2 score for Resonant Frequency 2 becomes negative (for example, $-0.0497$ for 40% test size). For higher test sizes, this shows that the model's predictions are worse than the mean of the actual values. Resonant Frequency 2 may be more difficult to model because of increased noise or nonlinearity in the data, as indicated by MAPE remaining between 4 and 5%, which suggests moderate percentage errors.

The design of an metamaterial absorber with target resonance frequencies and absorption efficiency greater than 90% was optimized using the suggested method. In comparison to traditional approaches, the regression based optimization method requires fewer evaluations and showed rapid convergence to the target resonant frequency and absorption percentage when the geometric parameters were adjusted within predetermined limits. The search was successfully directed into promising areas of the parameter space using the acquisition function. Important information about how sensitive the performance measurements were to each parameter was revealed by the posterior distributions. In contrast to the substrate width and back wire width, the split length was shown to have a more noticeable impact on both resonance frequency and absorption. From the error metrices comparison, it is clear that the prediction accuracy is quite high making it suitable for replacing traditional time consuming design method where computational resources requires is also very high.

## X. Physics Informed Confirmation And Tunability

Although the inverse regression models demonstrate strong quantitative performance, inverse design in metamaterials is inherently susceptible to non-uniqueness (i.e., multiple geometries can yield similar spectral signatures). Therefore, to ensure that the inverse-predicted geometric parameters correspond to physically valid absorber responses, we perform a physics-informed confirmation step using full-wave electromagnetic simulation.

In this validation, we first select three inverse-design test cases. For each case, a desired spectral response is specified in terms of the two resonance frequencies and corresponding absorption amplitudes, i.e., $\mathbf{y}^{\mathrm{des}} = [f_1^{\mathrm{des}}, f_2^{\mathrm{des}}, A_1^{\mathrm{des}}, A_2^{\mathrm{des}}]$. These desired values are then passed through the trained inverse regression surrogates to obtain the predicted geometry $\hat{\mathbf{x}} = [\hat{I}, \hat{IS}, \hat{S}]$ (with the remaining parameters fixed as described in Section IX). Next, the predicted geometry is imported into the same FEM simulation environment and boundary conditions used throughout this work. From the simulated absorption spectrum, we extract the two dominant resonance peaks and their peak absorption levels, yielding $\mathbf{y}^{\mathrm{sim}} = [f_1^{\mathrm{sim}}, f_2^{\mathrm{sim}}, A_1^{\mathrm{sim}}, A_2^{\mathrm{sim}}]$.

To quantify agreement between the inverse target and the physics-validated response, we compute the percentage error for each spectral component as

$$\epsilon_k(\%) = \left| \frac{y_k^{\mathrm{sim}} - y_k^{\mathrm{des}}}{y_k^{\mathrm{des}}} \right| \times 100, \quad k \in \{f_1, f_2, A_1, A_2\}. \tag{15}$$

We also report an overall validation error as the mean of the four component-wise percentage errors:

$$\bar{\epsilon}(\%) = \frac{1}{4} \sum_k \epsilon_k. \tag{16}$$

This physics-informed confirmation not only validates physical consistency but also emphasizes a crucial practical implication: tunability. The suggested framework makes it possible to directly retrieve the geometry needed to achieve that response because the inverse regression models accept a desired spectral specification as input (target resonance frequencies and peak absorption amplitudes). To put it another way, by choosing $\mathbf{y}^{\mathrm{des}} = [f_1^{\mathrm{des}}, f_2^{\mathrm{des}}, A_1^{\mathrm{des}}, A_2^{\mathrm{des}}]$, the inverse surrogate provides $\hat{\mathbf{x}} = [\hat{I}, \hat{IS}, \hat{IO}, \hat{S}]$ that can be immediately validated through full-wave simulation. Instead of depending on laborious manual sweeps, this creates a tunable absorber design path where the residual peaks and absorption levels can be purposefully changed by prescribing new desired values and carrying out inverse design.

The physics-informed confirmation results for the three inverse-predicted designs are compiled in Table VI and Fig. 10. The recovered peak locations and absorption magnitudes nearly match the expected values, resulting in very low percentage errors, and the full-wave simulated absorption spectra consistently replicate the intended dual-band behavior. As a result, the inverse regression models provide dependable and adjustable design for target spectral needs by producing geometries that are consistent under Maxwell-equation-based electromagnetic validation in addition to statistically accurate predictions. To position the present study with respect to representative THz absorber ML-assisted and other optimization based design approaches, a critical comparison is provided in TABLE VII.

## XI. Fabrication Feasibility and Experimental Prospects

The proposed dual-band THz metamaterial absorber is relevant to several practical application areas, particularly frequency-selective sensing, detection, filtering, and imaging-related spectral selection in the terahertz regime. It follows the fundamental metal–dielectric–metal THz metamaterial absorber configuration [16], which provides near-zero transmission, enhanced resonant absorption, and strong field confinement at the patterned surface. These same features also facilitate sensing by making the resonance highly sensitive to changes in the surrounding environment as demonstrated in our prior dual-band ITO-based absorber for biomedical refractive-index sensing [9], [75]. In detection, the absorber efficiently localizes incident THz energy into a lossy region that can be converted into a measurable signal, such as in the metamaterial absorber–micro-bolometer platform and later room-temperature metamaterial bolometers for low-power THz detection [76]. In imaging, absorber-based THz pixels can be scaled into focal-plane arrays to improve coupling efficiency and image formation [77], [78]. Finally, in stealth applications, THz metamaterial absorbers suppress reflected THz energy and reduce electromagnetic signature, with flexible absorber designs showing nearly 400-fold radar-cross-section reduction at THz range [79] and is being explored for cloaking technologies as well [80].

### *Fabrication Feasibility*

The presence of two strong and well-defined absorption resonances can be advantageous in applications requiring selective interaction at multiple frequencies, such as multi-band sensing or spectrally selective detection. From a practical implementation perspective, the present design is based on a planar metal–dielectric–metal resonator geometry on a dielectric substrate, which is

TABLE VI: Physics-informed confirmation of forward regression model: comparison between full-wave simulated responses and regression-predicted outputs for selected geometries.

| **Predicted Design / Geometry D** $\hat{\mathbf{x}} = [\hat{I}, \hat{S}, \hat{IO}, \hat{IS}]$ | **Simulated** $(f_1^{\text{sim}}, f_2^{\text{sim}}, A_1^{\text{sim}}, A_2^{\text{sim}})$ **from D** | **Desired Responses** $(f_1^{\text{des}}, f_2^{\text{des}}, A_1^{\text{des}}, A_2^{\text{des}})$ | **Error** $(\lvert\Delta f_1\rvert/f_1^{\text{sim}}, \lvert\Delta f_2\rvert/f_2^{\text{sim}})$ |
|---|---|---|---|
| Case 1: **D1** (13.6, 1.21, 3.99, 1.79) $\mu$m | $f_1^{\text{sim}} = 1.44$ THz<br>$f_2^{\text{sim}} = 4.205$ THz<br>$A_1^{\text{sim}} = 0.96$<br>$A_2^{\text{sim}} = 0.92$ | $f_1^{\text{des}} = 1.45$ THz<br>$f_2^{\text{des}} = 4.21$ THz<br>$A_1^{\text{des}} = 0.90$<br>$A_2^{\text{des}} = 0.90$ | $\lvert\Delta f_1\rvert/f_1^{\text{sim}} = 0.694\%$<br>$\lvert\Delta f_2\rvert/f_2^{\text{sim}} = 0.119\%$ |
| Case 2: **D2** (13.4, 1.19, 3.93, 1.78) $\mu$m | $f_1^{\text{sim}} = 1.445$ THz<br>$f_2^{\text{sim}} = 4.168$ THz<br>$A_1^{\text{sim}} = 0.97$<br>$A_2^{\text{sim}} = 0.94$ | $f_1^{\text{des}} = 1.45$ THz<br>$f_2^{\text{des}} = 4.17$ THz<br>$A_1^{\text{des}} = 0.98$<br>$A_2^{\text{des}} = 0.95$ | $\lvert\Delta f_1\rvert/f_1^{\text{sim}} = 0.346\%$<br>$\lvert\Delta f_2\rvert/f_2^{\text{sim}} = 0.048\%$ |
| Case 3: **D3** (13.5, 1.19, 4.49, 1.79) $\mu$m | $f_1^{\text{sim}} = 1.41$ THz<br>$f_2^{\text{sim}} = 4.21$ THz<br>$A_1^{\text{sim}} = 0.91$<br>$A_2^{\text{sim}} = 0.85$ | $f_1^{\text{des}} = 1.44$ THz<br>$f_2^{\text{des}} = 4.20$ THz<br>$A_1^{\text{des}} = 0.85$<br>$A_2^{\text{des}} = 0.85$ | $\lvert\Delta f_1\rvert/f_1^{\text{sim}} = 2.128\%$<br>$\lvert\Delta f_2\rvert/f_2^{\text{sim}} = 0.238\%$ |

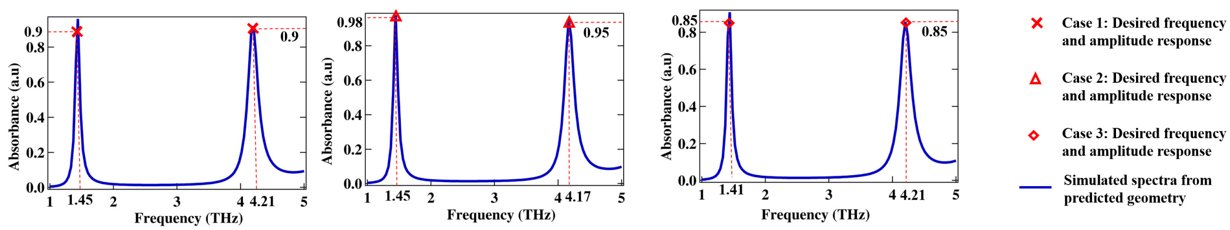


Fig. 10: Physics-informed confirmation of the inverse-design framework. Full-wave simulated absorption spectra (blue) obtained from regression-predicted geometries for three representative cases (Cases 1–3). Red symbols mark the desired resonance frequencies and corresponding peak absorption levels, while red dashed vertical lines indicate the target frequencies. The close match between the simulated spectra and the prescribed dual-band targets demonstrates physical validity and tunability of the proposed absorber.

conceptually compatible with commonly used microfabrication approaches for terahertz metamaterial absorbers [55]. Material losses are also inherently included in the electromagnetic model through the assigned conductive and dielectric properties used in the full-wave simulations [54]. The present study incorporates a simulation-driven optimization approach to guide the future fabrication and implementation of the proposed absorber. To further assess practical robustness, a fabrication-tolerance study was performed using the optimized design parameters. The results show that even with a 5% variation in the split-gap length, the simulated spectrum remains nearly identical to the nominal case, demonstrating that the optimized structure is reasonably tolerant to realistic fabrication imperfections. After applying a 5% variation to the split-length structural parameter as shown in Fig. 11, the simulated absorption spectra exhibit only negligible deviations, indicating that the overall device performance remains nearly unchanged. This result demonstrates that the proposed absorber design has strong fabrication tolerance, thereby confirming its practical feasibility for real-world implementation.

### *Experimental Prospects*

To further illustrate a practical realization pathway, Fig.12 shows a conceptual fabrication flow together with a representative reflection-mode terahertz time-domain spectroscopy (THz-TDS) setup for future experimental validation. As illustrated in Fig. 12(a), the absorber may be realized through a planar fabrication sequence involving resist patterning, metal deposition, and lift-off on the substrate. A future experimental characterization of the fabricated absorber may then be carried out using a commercial THz-TDS system in reflection mode, as illustrated in Fig. 12(b). In such a setup, a femtosecond fiber laser excites a biased photoconductive emitter to generate THz pulses, which are then focused onto the absorber sample using parabolic mirrors. The reflected THz signals are collected and directed to a photoconductive

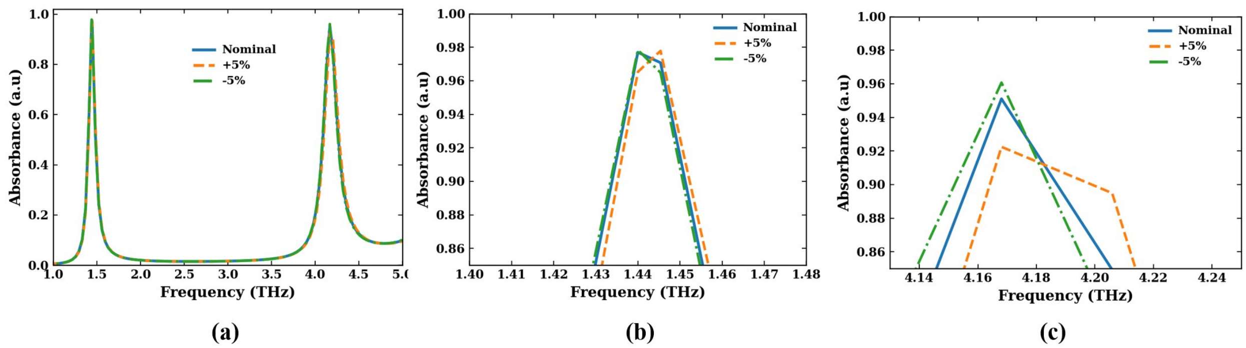


Fig. 11: Fabrication tolerance analysis of the proposed absorber under $\pm 5\%$ variation in the split-length parameter: (a) full absorption spectra, (b) enlarged view around the first resonance, and (c) enlarged view around the second resonance, showing only minor spectral changes and thus confirming good fabrication feasibility.

TABLE VII: Critical comparison of representative THz metamaterial absorber optimization studies and related design approaches with the present work.

| **Attribute** | **Wang et al. (2020) [51]** | **Abdulkarim et al. (2022) [52]** | **Soni and Misra (2023) [55]** | **Jain et al. (2024) [56]** | **Li et al. (2025) [57]** | **This work** |
|---|---|---|---|---|---|---|
| **Frequency range** | 0.1–3.0 THz | 0–1 THz | 0.1–6 THz | 13–16 THz | 0.2–1.2 THz | 0.5–5 THz |
| **Metastructure type** | Dual-band THz metal–dielectric–metal absorber with two identical square metallic patches | Dual-band THz metal–dielectric–metal absorber with Pythagorean tree fractal resonators on flexible PET substrate | Multiband metal–insulator–metal THz absorber with open polygon-shaped meta-atom | Dual square-ring metal–dielectric–metal THz absorber | Dual-band THz metal–dielectric–metal absorber with circular SRR nested in a swastika-inspired structure | Compact dual-band THz metal–dielectric–metal absorber with merged circular SRR |
| **ML methodology** | N/A | N/A | Forward and inverse ML using LR, KNN, DT, and NN | Forward regression using DT, KNN, RF, ET, Bagging, XGB, and CatBoost | Multi-objective evolutionary optimization | Forward and inverse design with tree based regression ML frameworks |
| **Dataset size** | N/A | N/A | ∼6000 simulated spectra | Sample count not explicitly stated | Optimization population size 15, maximum iterations 15 | 400 simulated samples containing 4 varied geometric input parameters |
| **Validation strategy** | Full-wave simulation, absorption analysis, impedance matching, field distribution, and sensing evaluation | Full-wave simulation, parameter optimization, sensing analysis, and experimental THz-TDS validation | MSE evaluation, epoch–loss monitoring, and full-wave re-simulation of inverse-predicted structures | Random train–test splits and MAE, MSE, and RMSE evaluation | Full-wave simulation | Multiple train–test splits (80:20, 70:30, 60:40) ( for validation and overfit check), MSE, RMSE, NRMSE etc. evaluation, and full-wave revalidation of inverse-predicted structures |
| **Key difference with the proposed work** | Depends on time-intensive simulation-driven optimization based on manual parametric sweeps | Before experimental validation, required computationally expensive trial-and-error based parameter sweeps | Higher-dimensional full-spectrum learning framework, lower feature-to-sample ratio, high computational cost | Forward-prediction-only framework, no inverse design and no closed-loop geometry revalidation | Search-based optimization study, not data-driven | Integrates structural simplicity with forward prediction and inverse geometric retrieval, low computational cost, high feature-to-sample ratio, and full-wave revalidation for practical spectrum-to-structure design |

detector to record the time-domain waveform, which can subsequently be transformed into the frequency domain using fast Fourier transform (FFT). To obtain reflectance, the sample response may be normalized to a reference measurement taken from a standard gold mirror. Such measurements are commonly performed in dry air to reduce undesired terahertz absorption by water vapor [55], [81].

## XI. Conclusion

In this work, a novel dual-band THz metamaterial absorber based on merged circular split-ring resonators was designed, simulated, and analyzed. The structure exhibited very strong absorption peaks near 1.44 THz and 4.24 THz. Electromagnetic properties, including effective permittivity, permeability, refractive index, impedance, and field distributions, confirmed the resonant behavior and absorption mechanism of the unit

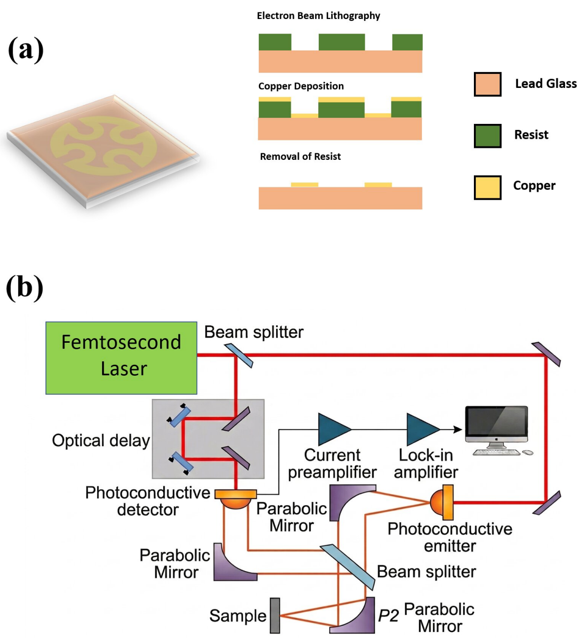


Fig. 12: Practical realization pathway of the proposed dual-band THz metamaterial absorber. (a) Conceptual planar fabrication flow of the absorber, illustrating resist patterning, copper deposition, and lift-off on the substrate (similar process applicable for bottom copper wire). (b) Representative reflection-mode terahertz time-domain spectroscopy (THz-TDS) setup for experimental characterization, including the femtosecond laser, beam splitters, optical delay, photoconductive emitter/detector, parabolic mirrors, and sample position.

cell. A parametric study was performed by varying key geometric parameters to generate a dataset of 373 simulations selected from 400 full-wave runs, enabling machine-learning-based forward and inverse design. Regression models accurately predicted spectral responses from geometry (forward mapping) and retrieved geometric configurations from desired resonance frequencies and absorption amplitudes (inverse mapping). To ensure physical reliability beyond statistical performance, a physics-informed confirmation step was carried out by re-simulating multiple inverse-predicted designs in a electromagnetic full-wave solver and comparing the extracted peak frequencies and absorption amplitudes with the intended target frequencies, yielding low percentage errors. This validation demonstrates the tunability of the proposed absorber, as the inverse design framework enables direct spectrum-to-structure synthesis for user-specified dual-band requirements. Overall, the proposed approach provides a robust and efficient route for rapid prototyping and optimization of THz absorbers while reducing dependence on computationally expensive iterative simulations.

## References


[1] V. G. Veselago, "The Electrodynamic of Substances with Simultaneous Negative Values of $\epsilon$ and $\mu$," *Soviet Physics Uspekhi*, vol. 10, no. 4, pp. 509–514, 1968.

[2] J. B. Pendry, A. J. Holden, D. J. Robbins, and W. J. Stewart, "Magnetism from conductors and enhanced nonlinear phenomena," *IEEE Transactions on Microwave Theory and Techniques*, vol. 47, no. 11, pp. 2075–2084, 1999.

[3] D. R. Smith, W. J. Padilla, D. C. Vier, S. C. Nemat-Nasser, and S. Schultz, "Composite medium with simultaneously negative permeability and permittivity," *Physical Review Letters*, vol. 84, pp. 4184–4187, may 2000.

[4] W. Cai, U. K. Chettiar, H.-K. Yuan, V. C. de Silva, A. V. Kildishev, V. P. Drachev, and V. M. Shalaev, "Metamagnetics with rainbow colors," *Optics Express*, vol. 15, no. 6, p. 3333, 2007.

[5] F. Younis, O. Khan, J. Ahmad, M. J. Qasim, H. Luo, and S. Wang, "A highly efficient triple band metasurface enabled absorber for 5g/6g millimeter wave applications," *Scientific Reports*, vol. 15, no. 1, p. 29455, 2025.

[6] M. R. Rakhshani, F. Kazemi, and M. Rashki, "Metamaterial absorber using cascaded ring resonators and optimization through machine learning for sensing applications," *Scientific Reports*, vol. 15, no. 1, p. 39977, 2025.

[7] A. S. Mohammed, A. Shohdy, S. A. Mohammed, and A. M. Montaser, "Design and optimization of a metamaterial absorber for enhanced solar cell efficiency and wide band microwave cross polarization conversion," *Scientific Reports*, vol. 15, no. 1, p. 31350, 2025.

[8] S. K. Ranjan and S. Sahoo, "Six band metamaterial absorber designed on twisted square and swastika-shaped resonator for s, c, x, and ku band frequency and sensing applications," *Physica Scripta*, vol. 100, no. 1, p. 015534, 2025.

[9] S. J. Mishu, M. A. Rahman, and N. Dhar, "Highly sensitive refractive index sensing with a dual-band optically transparent ito-based perfect metamaterial absorber for biomedical applications," *Heliyon*, vol. 10, no. 5, 2024.

[10] R. Bhati and A. K. Malik, "Multiband terahertz metamaterial perfect absorber for microorganisms detection," *Scientific Reports*, vol. 13, no. 1, p. 19685, 2023.

[11] J. M. Jornet and I. F. Akyildiz, "Femtosecond-long pulse-based modulation for terahertz band communication in nanonetworks," *IEEE Transactions on Communications*, vol. 62, no. 5, pp. 1742–1754, 2014.

[12] A. Shafie, N. Yang, S. A. Alvi, C. Han, S. Durrani, and J. M. Jornet, "Spectrum allocation with adaptive sub-band bandwidth for terahertz communication systems," *IEEE Transactions on Communications*, vol. 70, no. 2, pp. 1407–1422, 2021.

[13] C. Lin and G. Y. Li, "Adaptive beamforming with resource allocation for distance-aware multi-user indoor terahertz communications," *IEEE Transactions on Communications*, vol. 63, no. 8, pp. 2985–2995, 2015.

[14] S. Tarboush, A. Ali, and T. Y. Al-Naffouri, "Cross-field channel estimation for ultra massive-mimo thz systems," *IEEE Transactions on Wireless Communications*, vol. 23, no. 8, pp. 8619–8635, 2024.

[15] Z. Tang, N. Yang, S. Durrani, X. Zhou, M. Juntti, and J. M. Jornet, "Coverage analysis for 3d indoor terahertz communication system over multi-cluster fluctuating two-ray fading channels," *IEEE Transactions on Communications*, 2025.

[16] N. I. Landy, S. Sajuyigbe, J. J. Mock, D. R. Smith, and W. J. Padilla, "Perfect metamaterial absorber," *Physical Review Letters*, vol. 100, no. 20, pp. 1–4, 2008.

[17] J. Liu, W. Chen, W.-Z. Ma, Y.-S. Chen, X.-C. Deng, P.-P. Zhuang, and Q. Ye, "Biaxial hyperbolic metamaterial thz broadband absorber utilizing anisotropic two-dimensional materials," *Results in Physics*, vol. 22, p. 103818, 2021.

[18] A. Elakkiya, S. Radha, B. S. Sreeja, and E. Manikandan, "Terahertz metamaterial absorber with sensing capabilities," *Journal of Optoelectronics and Advanced Materials*, vol. 22, no. 7-8, pp. 360–364, 2020.

[19] Y. I. Abdulkarim, F. Özkan Alkurt, H. N. Awl, F. F. Muhammadsharif, M. Bakır, S. Dalgac, M. Karaaslan, and H. Luo, "An ultrathin and dual band metamaterial perfect absorber based on ZnSe for the polarization-independent in terahertz range," *Results in Physics*, vol. 26, no. May, p. 104344, 2021.

[20] B.-X. Wang, W. Zhou, Q. Zhao, H. Wang, Y. Zhang, D.-Q. Zhang, F.-Z. Shu, G. Yang, and L. Wu, "Ge2sb2te5-based multifunctional reconfigurable terahertz metamaterials with joint polarization control," *Laser & Photonics Reviews*, p. e02941, 2025.

[21] Y. Zou, R. Luo, S. Chen, S. Zhou, and Z. Fan, "Terahertz spatial light modulation by phase change metasurface with pixel-wise switchable control," *Optics Express*, vol. 32, no. 21, pp. 36261–36271, 2024.

[22] T. M. Nguyen, D. L. Vu, T. Q. H. Nguyen, and J.-M. Kim, "Reconfigurable broadband metasurfaces with nearly perfect absorption and high efficiency polarization conversion in thz range," *Scientific Reports*, vol. 12, no. 1, p. 18779, 2022.

[23] X. Hou, X. Chen, T. Li, Y. Li, Z. Tian, and M. Wang, "Highly sensitive terahertz metamaterial biosensor for bovine serum albumin (BSA) detection," *Optical Materials Express*, vol. 11, no. 7, p. 2268, 2021.

[24] S. J. Mishu, M. A. Rahman, and N. Dhar, "High fom quad-band thz perfect metamaterial absorber-based ri sensor for gas sensing applications," *Electronics Letters*, vol. 60, no. 10, p. e13223, 2024.

[25] C. Shi, X. F. Zang, L. Chen, Y. Peng, B. Cai, G. R. Nash, and Y. M. Zhu, "Compact broadband terahertz perfect absorber based on multi-interference and diffraction effects," *IEEE Transactions on Terahertz Science and Technology*, vol. 6, no. 1, pp. 40–44, 2015.

[26] S. Barzegar-Parizi, A. Ebrahimi, and K. Ghorbani, "Two bits dual-band switchable terahertz absorber enabled by composite graphene and vanadium dioxide metamaterials," *Scientific Reports*, vol. 14, no. 1, p. 5818, 2024.

[27] M. Amiri, F. Tofigh, N. Shariati, J. Lipman, and M. Abolhasan, "Wide-angle metamaterial absorber with highly insensitive absorption for TE and TM modes," *Scientific Reports*, vol. 10, no. 1, pp. 1–13, 2020.

[28] S. Kumar and D. K. Aswal, *Thin Film and Significance of Its Thickness*, pp. 1–12. Singapore: Springer Singapore, 2020.

[29] N. Singh, R. Dhara, and S. Yadav, "Design and optimization of a polarization-insensitive terahertz metamaterial absorber for sensing applications," *Photonics and Nanostructures-Fundamentals and Applications*, vol. 62, p. 101314, 2024.

[30] K. Aliqab, A. Armghan, and M. Alsharari, "Polarization insensitive and wideband terahertz absorber using high-impedance resistive material of ruo2," *Scientific Reports*, vol. 14, no. 1, p. 19149, 2024.

[31] E. Sharifi, M. Razaghi, and K. Hosseini, "Ann assisted design of broadband near perfect metasurface absorbers exploiting inas nanorods for visible light harvesting," *Scientific Reports*, vol. 15, no. 1, p. 31060, 2025.

[32] R. Li Voti, "Optimization of a perfect absorber multilayer structure by genetic algorithms," *Journal of the European Optical Society*, vol. 14, pp. 1–12, dec 2018.

[33] Z. Li, M. Cheng, A. Tyrrell, and X. Zhao, "A Review of Data-Driven Models for Electromagnetic Devices Design and Analysis," *IEEE Access*, 2025.

[34] H. H. Park, H. Lee, and D. K. Hwang, "Regression Analysis for Predicting the Magnetic Field Shielding Effectiveness of Ferrite Sheets," *Electronics (Switzerland)*, vol. 14, jan 2025.

[35] S. Koziel and M. Abdullah, "Machine-Learning-Powered EM-Based Framework for Efficient and Reliable Design of Low Scattering Metasurfaces," *IEEE Transactions on Microwave Theory and Techniques*, vol. 69, pp. 2028–2041, apr 2021.

[36] M. Nazari, Y. M. Banad, and S. Sharif, "Inverse designed aperiodic multilayer perfect absorbers for mid infrared enable tunability switchability and angular robustness," *Scientific Reports*, vol. 15, no. 1, p. 17614, 2025.

[37] T. Zhang, Q. Liu, Y. Dan, S. Yu, X. Han, J. Dai, and K. Xu, "Machine learning and evolutionary algorithm studies of graphene metamaterials for optimized plasmon-induced transparency," *Optics Express*, vol. 28, no. 13, pp. 18899–18916, 2020.

[38] S. Ijaz, S. Noureen, B. Rehman, O. Aldaghri, H. Cabrera, K. H. Ibnaouf, N. Madkhali, and M. Q. Mehmood, "Machine-learning-driven accelerated design-method for meta-devices," *Materials Today Communications*, vol. 37, p. 106951, 2023.

[39] S. S. Sharif and Y. M. Banad, "Revolutionizing infrared detection in defense applications: A nanophotonic approach leveraging 2d materials for enhanced mid-ir absorption," in *2024 IEEE Research and Applications of Photonics in Defense Conference (RAPID)*, pp. 1–2, IEEE, 2024.

[40] G. Moon, J.-r. Choi, C. Lee, Y. Oh, K. H. Kim, and D. Kim, "Machine learning-based design of meta-plasmonic biosensors with negative index metamaterials," *Biosensors and Bioelectronics*, vol. 164, p. 112335, 2020.

[41] Z. Yang and M. J. Buehler, "High-throughput generation of 3d graphene metamaterials and property quantification using machine learning," *Small Methods*, vol. 6, no. 9, p. 2200537, 2022.

[42] D. Ebrahimzadeh, S. S. Sharif, and Y. M. Banad, "Accelerated discovery of vanadium oxide compositions: A wgan-vae framework for materials design," *Materials Today Electronics*, vol. 13, p. 100155, 2025.

[43] S. Sharif, "Evolutionary-based inverse design of 2d materials multilayer structures for next-generation ir smart sensing," in *Quantum Sensing and Nano Electronics and Photonics XXI*, vol. 13376, pp. 138–142, SPIE, 2025.

[44] J. R. Rokde and A. G. Thosar, "Linear regression approach for performance evaluation of ES with load impedance variations of non-critical and critical load," *e-Prime - Advances in Electrical Engineering, Electronics and Energy*, vol. 6, p. 100312, dec 2023.

[45] P. Jain, H. Chhabra, U. Chauhan, K. Prakash, P. Samant, D. K. Singh, M. S. Soliman, and M. T. Islam, "Machine learning techniques for predicting metamaterial microwave absorption performance: A comparison," *IEEE Access*, vol. 11, pp. 128774–128783, 2023.

[46] Z. Chen, A. Ogren, C. Daraio, L. C. Brinson, and C. Rudin, "How to see hidden patterns in metamaterials with interpretable machine learning," *Extreme Mechanics Letters*, vol. 57, p. 101895, 2022.

[47] W. Ji, J. Chang, H.-X. Xu, J. R. Gao, S. Gröblacher, H. P. Urbach, and A. J. Adam, "Recent advances in metasurface design and quantum optics applications with machine learning, physics-informed neural networks, and topology optimization methods," *Light: Science & Applications*, vol. 12, no. 1, p. 169, 2023.

[48] X. Jue, Y. Wang, Z. Xie, D. Han, S. Li, and J. Chen, "An efficient on-demand inverse design of terahertz metasurfaces via deep learning," *Optics & Laser Technology*, vol. 192, p. 113723, 2025.

[49] F. Zhao, P. Dong, K. Li, M. Zhang, W. Hou, and V. Melikyan, "Inverse design of terahertz metasurfaces for multi-channel holographic imaging based on the modified gradient descent method," *Optics Express*, vol. 33, no. 8, pp. 18005–18016, 2025.

[50] S. Yin, H. Zhong, W. Huang, and W. Zhang, "Deep learning enabled design of terahertz high-q metamaterials," *Optics & Laser Technology*, vol. 181, p. 111684, 2025.

[51] M. Soni and S. Misra, "Machine-learning-assisted design of multiband terahertz metamaterial absorber," *ACS Applied Optical Materials*, vol. 1, no. 10, pp. 1679–1687, 2023.

[52] P. Jain, M. T. Islam, and A. S. Alshammari, "Comparative analysis of machine learning techniques for metamaterial absorber performance in terahertz applications," *Alexandria Engineering Journal*, vol. 103, pp. 51–59, 2024.

[53] G. Li, Y. Huang, Y. Wang, W. Qu, H. Deng, and L. Shang, "Efficient design of a terahertz metamaterial dual-band absorber using multi-objective firefly algorithm based on a multi-cooperative strategy," in *Photonics*, vol. 12, p. 637, MDPI, 2025.

[54] B.-X. Wang, Y. He, P. Lou, and W. Xing, "Design of a dual-band terahertz metamaterial absorber using two identical square patches for sensing application," *Nanoscale Advances*, vol. 2, no. 2, pp. 763–769, 2020.

[55] Y. I. Abdulkarim, O. Altintas, A. S. Karim, H. N. Awl, F. F. Muhammadsharif, F. O. Alkurt, M. Bakir, B. Appasani, M. Karaaslan, and J. Dong, "Highly sensitive dual-band terahertz metamaterial absorber for biomedical applications: simulation and experiment," *ACS omega*, vol. 7, no. 42, pp. 38094–38104, 2022.

[56] S. Asgari and T. Fabritius, "Multi-band terahertz anisotropic metamaterial absorber composed of graphene-based split square ring resonator array featuring two gaps and a connecting bar," *Scientific Reports*, vol. 14, no. 1, p. 7477, 2024.

[57] Z. Wu, J. Tian, and R. Yang, "A graphene based dual-band metamaterial absorber for te polarized thz wave," *Micro and Nanostructures*, vol. 168, p. 207331, 2022.

[58] T. Lv, G. Dong, C. Qin, J. Qu, B. Lv, W. Li, Z. Zhu, Y. li, C. Guan, and J. Shi, "Switchable dual-band to broadband terahertz metamaterial absorber incorporating a vo2 phase transition," *Optics Express*, vol. 29, pp. 5437–5447, 02 2021.

[59] H. Li, W. Xu, Q. Cui, Y. Wang, and J. Yu, "Theoretical design of a reconfigurable broadband integrated metamaterial terahertz device," *Opt. Express*, vol. 28, pp. 40060–40074, Dec 2020.

[60] S. Asgari and T. Fabritius, "Multi-band terahertz graphene-based anisotropic metamaterial absorber comprised of two circular split ring resonator arrays with two gaps and a connection rod," *Optical and Quantum Electronics*, vol. 57, no. 3, pp. 1–18, 2025.

[61] Y. Liu, R. Huang, and Z. Ouyang, "Numerical investigation of graphene and sto based tunable terahertz absorber with switchable bifunctionality of broadband and narrowband absorption," *Nanomaterials*, vol. 11, no. 8, 2021.

[62] D. Wang, K.-D. Xu, S. Luo, Y. Cui, L. Zhang, and J. Cui, "A high q-factor dual-band terahertz metamaterial absorber and its sensing characteristics," *Nanoscale*, vol. 15, no. 7, pp. 3398–3407, 2023.

[63] A. SELLIER, T. Teperik, and A. de Lustrac, "Resonant circuit model for efficient metamaterial absorber," *Optics Express*, vol. 21, pp. A997–A1006, 10 2013.

[64] F. Costa, S. Genovesi, A. Monorchio, and G. Manara, "A circuit-based model for the interpretation of perfect metamaterial absorbers," *IEEE Transactions on Antennas and Propagation*, vol. 61, no. 3, pp. 1201–1209, 2013.

[65] Y. Pang, H. Cheng, Y. Zhou, and J. Wang, "Analysis and design of wire-based metamaterial absorbers using equivalent circuit approach," *Journal of Applied Physics*, vol. 113, p. 114902, 03 2013.

[66] A. Sellier, T. V. Teperik, and A. de Lustrac, "Resonant circuit model for efficient metamaterial absorber," *Optics express*, vol. 21, no. S6, pp. A997–A1006, 2013.

[67] F. Costa, S. Genovesi, A. Monorchio, and G. Manara, "A circuit-based model for the interpretation of perfect metamaterial absorbers," *IEEE Transactions on Antennas and Propagation*, vol. 61, no. 3, pp. 1201–1209, 2012.

[68] Y. Pang, H. Cheng, Y. Zhou, and J. Wang, "Analysis and design of wire-based metamaterial absorbers using equivalent circuit approach," *Journal of Applied Physics*, vol. 113, no. 11, 2013.

[69] Y. Luo, K. Qiu, T. Xu, F. Zhang, and P. Yue, "Design of a novel multiband terahertz metamaterial absorber using a deep learning framework," *Engineering Applications of Artificial Intelligence*, vol. 151, p. 110801, 2025.

[70] L. Meier, S. Van De Geer, and P. Bühlmann, "The group lasso for logistic regression," *Journal of the Royal Statistical Society Series B: Statistical Methodology*, vol. 70, no. 1, pp. 53–71, 2008.

[71] W.-Y. Loh, "Classification and regression trees," *Wiley interdisciplinary reviews: data mining and knowledge discovery*, vol. 1, no. 1, pp. 14–23, 2011.

[72] U. Grömping, "Variable importance assessment in regression: linear regression versus random forest," *The American Statistician*, vol. 63, no. 4, pp. 308–319, 2009.

[73] J. H. Friedman, "Greedy function approximation: a gradient boosting machine," *Annals of statistics*, pp. 1189–1232, 2001.

[74] D. Liu, Y. Tan, E. Khoram, and Z. Yu, "Training deep neural networks for the inverse design of nanophotonic structures," *Acs Photonics*, vol. 5, no. 4, pp. 1365–1369, 2018.

[75] S. Ahmed, T. Alam, M. M. Soliman, A. M. Moubark, M. M. Rahman, M. S. Islam, and M. T. Islam, "Enhanced structural tunability and high sensitivity of a thz metasurface absorber for precise automotive fuel characterization," *Scientific Reports*, vol. 15, no. 1, p. 22996, 2025.

[76] J. Grant, I. Escorcia-Carranza, C. Li, I. J. McCrindle, J. Gough, and D. R. Cumming, "A monolithic resonant terahertz sensor element comprising a metamaterial absorber and micro-bolometer," *Laser & Photonics Reviews*, vol. 7, no. 6, pp. 1043–1048, 2013.

[77] I. E. Carranza, J. P. Grant, J. Gough, and D. Cumming, "Terahertz metamaterial absorbers implemented in cmos technology for imaging applications: scaling to large format focal plane arrays," *IEEE Journal of Selected Topics in Quantum Electronics*, vol. 23, no. 4, pp. 1–8, 2016.

[78] J. Xu, J. Miao, Y. Liu, and X. Yu, "Performance enhanced terahertz imaging using a high-response thermomechanical microcantilever fpa," *Infrared Physics & Technology*, vol. 123, p. 104161, 2022.

[79] K. Iwaszczuk, A. C. Strikwerda, K. Fan, X. Zhang, R. D. Averitt, and P. U. Jepsen, "Flexible metamaterial absorbers for stealth applications at terahertz frequencies," *Optics express*, vol. 20, no. 1, pp. 635–643, 2011.

[80] H. Tao, N. Landy, K. Fan, A. Strikwerda, W. Padilla, R. Averitt, and X. Zhang, "Flexible terahertz metamaterials: Towards a terahertz metamaterial invisible cloak," in *2008 IEEE International Electron Devices Meeting*, pp. 1–4, IEEE, 2008.

[81] Z. Shen, S. Li, Y. Xu, W. Yin, L. Zhang, and X. Chen, "Three-dimensional printed ultrabroadband terahertz metamaterial absorbers," *Physical Review Applied*, vol. 16, no. 1, p. 014066, 2021.

## FUNDINGS

This research is based upon work supported by the Office of Naval Research under award number N000142512293.

## AUTHOR CONTRIBUTIONS

SM conceptualized the original idea, performed all electromagnetic simulations, and drafted the initial manuscript. SS and YB supervised the project, provided direction on refining the concept and further developing the physics-informed design section, and critically reviewed and edited the manuscript for technical accuracy. All authors (SM, SS, and YB) contributed equally to the final manuscript.

## DATA AVAILABILITY

The datasets generated during and/or analyzed during the current study are made publicly available. Click here.

## DECLARATIONS

The authors declare no competing interests

## COMPETING INTERESTS

The authors declare no competing interests.